Nucleon-Nucleon Optical Model for Energies to 3 GeV

A. Funk[1]*, H.V. von Geramb[1,2] †and K.A. Amos[2] ‡

[1] Theoretische Kernphysik, Universität Hamburg,
Luruper Chaussee 149, D-22761 Hamburg, Germany

[2] School of Physics, University of Melbourne,
Victoria 3010, Australia

April 30, 2001

Abstract

Several nucleon-nucleon potentials, Paris, Nijmegen, Argonne, and those derived by quantum inversion, which describe the NN interaction for $T_{Lab} \leq 300$ MeV are extended in their range of application as NN optical models. Extensions are made in r-space using complex separable potentials definable with a wide range of form factor options including those of boundary condition models. We use the latest phase shift analyses SP00 (FA00, WI00) of Arndt *et al.* from 300 MeV to 3 GeV to determine these extensions. The imaginary parts of the optical model interactions account for loss of flux into direct or resonant production processes. The optical potential approach is of particular value as it permits one to visualize fusion, and subsequent fission, of nucleons when $T_{Lab} > 2$ GeV. We do so by calculating the scattering wave functions to specify the energy and radial dependences of flux losses and of probability distributions. Furthermore, half-off the energy shell t-matrices are presented as they are readily deduced with this approach. Such t-matrices are required for studies of few- and many-body nuclear reactions.

1 Introduction

A theoretical description of nucleon-nucleon (NN) scattering is a fundamental ingredient for the understanding of nuclear structure and scattering of few- and many-body nuclear systems [1, 2, 3]. This is a paradigm of nuclear physics. Of the spectrum, low energy NN scattering

*funk@physnet2.uni-hamburg.de
†geramb@uni-hamburg.de
‡amos@higgs.ph.unimelb.edu.au

traditionally is described in terms of few degrees of freedom of which spin and isospin symmetries play the predominant role. At medium energies, production processes and inelasticities become important and several elementary systems composed of nucleons and mesons contribute to NN scattering. While these nucleons and mesons are emergent structures from QCD, at present there is no quantitative description of NN scattering above the inelastic threshold either in terms of QCD or of the emergent nucleons and mesons [4].

Theoretically undisputed is the need for relativity [5] of which there are two aspects. First is the increasing importance of relativistic kinematics as the kinetic energy becomes comparable to the rest masses of the scattering particles. Second, particle production is inherently relativistic requiring, ultimately, a description in terms of highly non-linear QCD. But that non-linearity inhibits a facile QCD explanation of NN scattering. Notwithstanding, there exist hybrid models which offset that non-linearity in seeking explanation of the excitation spectra and of the scattering of hadrons [6, 7]. All use heavy valence quarks, with an effective mass typically of 300 MeV, and massive Goldstone bosons in lieu of massless gluons. They also maintain color degrees of freedom. As well there are effective quantum field theories (EQF) that link the quark-gluon structure of the standard model to low energy nuclear physics [8, 9]. Currently these latter approaches are very popular as they may give a foundation and interpretation of emergent structures. But like the hybrid models, due to the underlying expansion schemes used with EQF, many *ad hoc* degrees of freedom are involved.

The experimental NN data and its parameterization in terms of amplitudes and phase shifts, are very smooth with energy to 3 GeV [10, 11, 12]; a feature which supports use of the *classic* approach using a free NN interaction potential. By so doing one uses a minimal number of degrees of freedom with again those degrees of freedom being associated with the spin and isospin of the total system. Of course, this *classic* approach sacrifices all reliance on substructures. However, the underlying dynamic still reflects its geometric facet by means of surfaces and boundary conditions. The success of bag models is direct evidence of the crucial role such boundary conditions play with the emergent structures from them being direct consequences of QCD confinement. This is further support for our view that an explanation of elastic NN scattering need not, if will not, depend explicitly upon QCD details. Only geometric attributes of the QCD domain, we contend, are required to explain most data. This view is well supported by high energy scattering for which the geometric limits of the S-matrix are reached and form factors are defined independent of energy. In the transition region the geometric limits are not reached and the factorization schemes [13, 14] used at higher energies do not apply.

Of course, in the last decade or so, there have been several theoretical attempts built upon boson exchange models to explain NN scattering data to 1 GeV. All such have given but qualitative results, often requiring many degrees of freedom even to achieve that qualitative agreement and despite explicit inclusion of Δ and N^* resonances. Optical model studies have also been made for medium and modest high energy NN scattering [15, 16, 17], and they can be improved to give a high quality description of scattering at medium energy.

A high quality fit of on-shell t-matrices by a potential model is very desirable also as it facilitates extension into the off-shell domain; properties which are needed in few and many body

calculations. In particular, microscopic optical model potentials for elastic nucleon-nucleus scattering and bremsstrahlung reactions that give quantitative results, require a careful and exact treatment of the off-shell NN t-matrices [18]. Furthermore, calculations of such entities have shown that it is crucial to have on-shell values of the t-matrices in best possible agreement with NN data at all energies. Concomitantly one needs high precision NN data against which one can specify NN interactions.

There are many studies of few and many body problems in the low energy regime $T_{Lab} < 300$ MeV and the results have consequences for any model extension above threshold [3]. We note in this context that significant off-shell differences in t-matrices are known to exist between the theoretically well motivated boson exchange models of NN scattering in this regime. It remains difficult to attribute with certainty any particular dynamical or kinematical feature with those differences. Non-locality, explicit energy dependence and features associated with relativistic kinematics are some possibilities.

In contrast, there is the quantum inverse scattering approach by which any on-shell t-matrix can be continued into the off-shell domain [19]. A specific method is the Gel'fand–Levitan–Marchenko inversion algorithm for Sturm–Liouville equations. This approach to specify t-matrices off-shell is appropriate when the physical S-matrix is unitary and the equation of motion is of the Sturm–Liouville type. Such is valid without modification for NN t-matrices in the energy regime to 300 MeV. Mathematically, the Gel'fand–Levitan–Marchenko algorithm is a method based upon a class of real and regular potentials. In the spirit of inverse scattering, we generalize that method for non-unitary S-matrices. By that means we generate an NN optical model separately for each partial wave. The algorithm we have developed allows studies of complex separable potentials in combination with any background potential. The background potential can be any of the existing r-space *NN* potentials. We have not used k-space background potentials, such as Bonn-B [2], Bonn-CD [20] and OSBEP [21], albeit that similar analyses can be made with them.

We limit the reference potential to the well known real r-space potentials from Paris [22], Nijmegen [23] (Reid93, Nijmegen-I, Nijmegen-II), Argonne [24] (AV18), and from inversion [25, 26]. To them we add channel dependent complex separable potentials with energy dependent strengths. For given input data results then, the full potentials are unique. The experimental background and motivation for analyses using an optical model is given in Sect. II. A detailed description of the theoretical algorithm is given in Sect. III. A discussion of results is given in Sect. IV while a summary is given in Sect. V.

2 Survey of data and motivation for the optical potential

NN scattering is a long standing problem which has been reviewed often as the database developed [10, 11, 20, 27]. The low energy data has been analyzed by the VPI/GWU group [12] for $T_{Lab} \leq 400$ MeV, the Nijmegen group [27] with the NN phase shift results PWA93 for $T_{Lab} \leq 350$ MeV, and by Machleidt [20] giving the Bonn-CD-2000. Of these, the VPI/GWU

group has given many solutions for this low energy regime over the years, all of which have been listed by Arndt *et al.* in a very recent publication [12]. For their use note that the solution name reflects the season and year of their creation although the low energy solutions have names that end with 40. Clearly that database has grown rapidly in the last two decades. While the *pp* data now extends to 3 GeV, the *np* data are limited to 1.3 GeV. Surprisingly, the solutions from SM97 to WI00 remain very closely the same and are very stable with regard to new data. We have used the solutions SP00, FA00 and WI00 in our calculations and found results that differ but marginally. Thus hereafter in the main we refer solely to the results of calculations based upon SP00. The findings are equally valid for other more recently dated solutions. In our practical applications however when new potentials are sought their generation is based upon the most current solution [28].

The VPI/GWU solutions [29] are parameterizations of the elastic channel NN S-matrix. They consider

$$S_1 = (1 + iK_4)(1 - iK_4)^{-1} \tag{1}$$

which inverts to give

$$K_4 = i(1 - S_1)(1 + S_1)^{-1} = Re\, K_4 + iIm\, K_4. \tag{2}$$

The real part of this K-matrix is related to a unitary S-matrix (S_6) and therewith phase shifts $\delta^{\pm}$ and ϵ are defined by

$$S_6 = \frac{(1 + i\, Re\, K_4)}{(1 - i\, Re\, K_4)} = \left\{ \begin{array}{cc} \cos 2\varepsilon \exp 2i\delta^- & i \sin 2\varepsilon \exp i(\delta^- + \delta^+) \\ i \sin 2\varepsilon \exp i(\delta^- + \delta^+) & \cos 2\varepsilon \exp 2i\delta^+ \end{array} \right\}. \tag{3}$$

The absorption parameters $\rho^{\pm}$ and μ relate to the imaginary part of that K-matrix by

$$Im\, K_4 = \left\{ \begin{array}{cc} \tan^2 \rho^- & \tan \rho^- \tan \rho^+ \cos \mu \\ \tan \rho^- \tan \rho^+ \cos \mu & \tan^2 \rho^+ \end{array} \right\}. \tag{4}$$

These relations simplify to $K = \tan \delta + i \tan^2 \rho$ for uncoupled channels.

In our study, real NN potentials derived from fixed angular momentum inverse scattering theory have been used. They have been generated from inversion algorithms predicated upon the Gel'fand–Levitan–Marchenko integral equations which physically link to the radial Schrödinger equation of a fixed angular momentum,

$$\left[-\frac{d^2}{dr^2} + \frac{\ell(\ell+1)}{r^2} + \frac{2\mu}{\hbar^2} V_\ell(r) \right] \psi_\ell(r,k) = k^2 \psi_\ell(r,k), \tag{5}$$

where $V_\ell(r)$ is a local and energy independent operator in coordinate space. Substituting

$$q(r) = \frac{\ell(\ell+1)}{r^2} + \frac{2\mu}{\hbar^2} V_\ell(r), \quad \text{and} \qquad \lambda = k^2, \tag{6}$$

identifies Eq. (5) as a Sturm–Liouville equation

$$\left[-\frac{d^2}{dx^2} + q(x)\right] y(x) = \lambda y(x). \tag{7}$$

There are two equivalent inversion algorithms for the Sturm–Liouville equation, which one identifies as the Marchenko and the Gel'fand–Levitan inversion. Both yield principally the same solution and numerically they are complementary. The salient features are outlined for the case of uncoupled channels. For coupled channels the inversion equations are matrix equations with input and translation kernels correspondingly generalized.

In the Marchenko inversion the experimental information enters via the S-matrix, $S_\ell(k) = \exp(2i\delta_\ell(k))$, with which an input kernel is defined in the form of a Fourier-Hankel transform

$$F_\ell(r,t) = -\frac{1}{2\pi}\int_{-\infty}^{+\infty} h_\ell^+(rk)\,[S_\ell(k) - 1]\,h_\ell^+(tk)dk, \tag{8}$$

where $h_\ell^+(x)$ are Riccati-Hankel functions. This input kernel when used in the Marchenko equation,

$$A_\ell(r,t) + F_\ell(r,t) + \int_r^\infty A_\ell(r,s)F_\ell(s,t)ds = 0, \tag{9}$$

specifies the translation kernel $A_\ell(r,t)$. The potential of Eq. (5) is a boundary condition for that translational kernel,

$$V_\ell(r) = -2\frac{d}{dr}A_\ell(r,r). \tag{10}$$

The Gel'fand–Levitan inversion requires not the S-matrix but rather the Jost-function as spectral input. The latter is related to the S-matrix by

$$S_\ell(k) = \frac{F_\ell(-k)}{F_\ell(k)}. \tag{11}$$

The Gel'fand–Levitan input kernel then is defined as the Fourier-Bessel transform

$$G_\ell(r,t) = \frac{2}{\pi}\int_0^\infty j_\ell(rk)\left[\frac{1}{|F_\ell(k)|^2} - 1\right] j_\ell(tk)dk, \tag{12}$$

where $j_\ell(x)$ are Riccati-Bessel functions. The Gel'fand–Levitan integral equation

$$K_\ell(r,t) + G_\ell(r,t) + \int_0^r K_\ell(r,s)G_\ell(s,t)ds = 0, \tag{13}$$

also defines a translational kernel with boundary condition

$$V_\ell(r) = 2\frac{d}{dr}K_\ell(r,r). \tag{14}$$

The boundary conditions Eq. (10) and (14) yield identical potentials.

Determination of the input kernels from data, phase shift functions $\delta(T_{Lab}(k))$, or K-matrices $K(T_{Lab}(k))$, requires an accurate interpolation and extrapolation of that data. In all practical applications rational functions are very appropriate. In this work we made a representation of data for $T_{Lab}(k) \leq 3$ GeV where the order N of the rational functions $P^{[2N-1,2N]}(k)$ was chosen to be as small as possible. Typically $2 < N < 6$. An implication is that extrapolations of $\delta(k)$ from the highest energy (last) data point k_{max} to infinity do not change sign and $\lim_{k\to\infty} \delta(k) \sim 1/k$. We control the rational function fit with weight functions which guarantee that those fits will be particularly accurate for some desired interval and less stringent elsewhere. For example, the channels $^1S_0$, $^1P_1$, $^3P_{0,1}$, $^3D_2$ and $^1F_3$ were weighted with $w_{Low} = 1$ for $T_{Lab} < 1.2$ GeV and for larger energies, $w_{High} = 0.05$. For the $^1D_2$ and $^3F_3$ channels, the cut between w_{Low} and w_{High} was 300 MeV. Consequently the rational functions used in the inversion algorithm ensure that the resulting potentials will give the desired values of phase shifts from solutions of the Schrödinger equation. Such is evident from the comparisons given in Figs. 1 and 2. Therein the fits to the phase shifts to 300 MeV resulting from all three models are considered as high quality. Single and coupled channel phase shifts from SM97 and FA00 solutions for $J \leq 3$ are shown together with values found from calculations made using three potential models. These model phase shifts were generated with Nijmegen-I and Nijmegen-II [23], and Argonne AV18 [24] interactions, and with potentials determined using Gel'fand–Levitan–Marchenko inversion[17, 25, 26].

On the scale to 3 GeV the OBE model results clearly diverge from data. As with the phase shift analyses, OBE potentials have received several critical reviews[3, 20], including observations that there are small variations between phase shift analyses and potential model results in the subthreshold domain $T_{Lab} < 300$ MeV [30]. A theoretically stable result would require many quantities, that need be specified *a priori*, to be determined from other sources. At present that does not seem feasible and all current potentials rely upon fits of many of their parameters to the same data. All such fits, however, have been made independently of each other and are based upon differing theoretical specifications of the boson exchange model dynamics. In Figs. 3 and 4 we give a quantitative demonstration of the ensuing differences. Therein the Nijmegen phase shift analysis PWA93 [27] has been used as reference values for various other phase shift solutions and potential predictions for the np $^1S_0$, and $^3P_0$ channels. Such differences are characteristic of variations between finite power series expansions of data in a finite interval. A mathematical property of such finite power series expansions within an interval is that, while the data in the interval will be well reproduced, continuations beyond that interval can radically diverge. Such a property is in evidence in Figs. 1 and 2, and that variance is the reason for the caveat often espoused that use of OBEP beyond the fitted energy range should be prohibited. Be that as it may, one could expect from a consistent theory that such extrapolations, albeit in error, would be the same. Clearly they are not. However of one thing we can be sure, the lack of physics with these models lies within the interaction distance < 1 fm. The optical model approach we present is an attempt within the frame of potential scattering theory to account for and identify such short range properties.

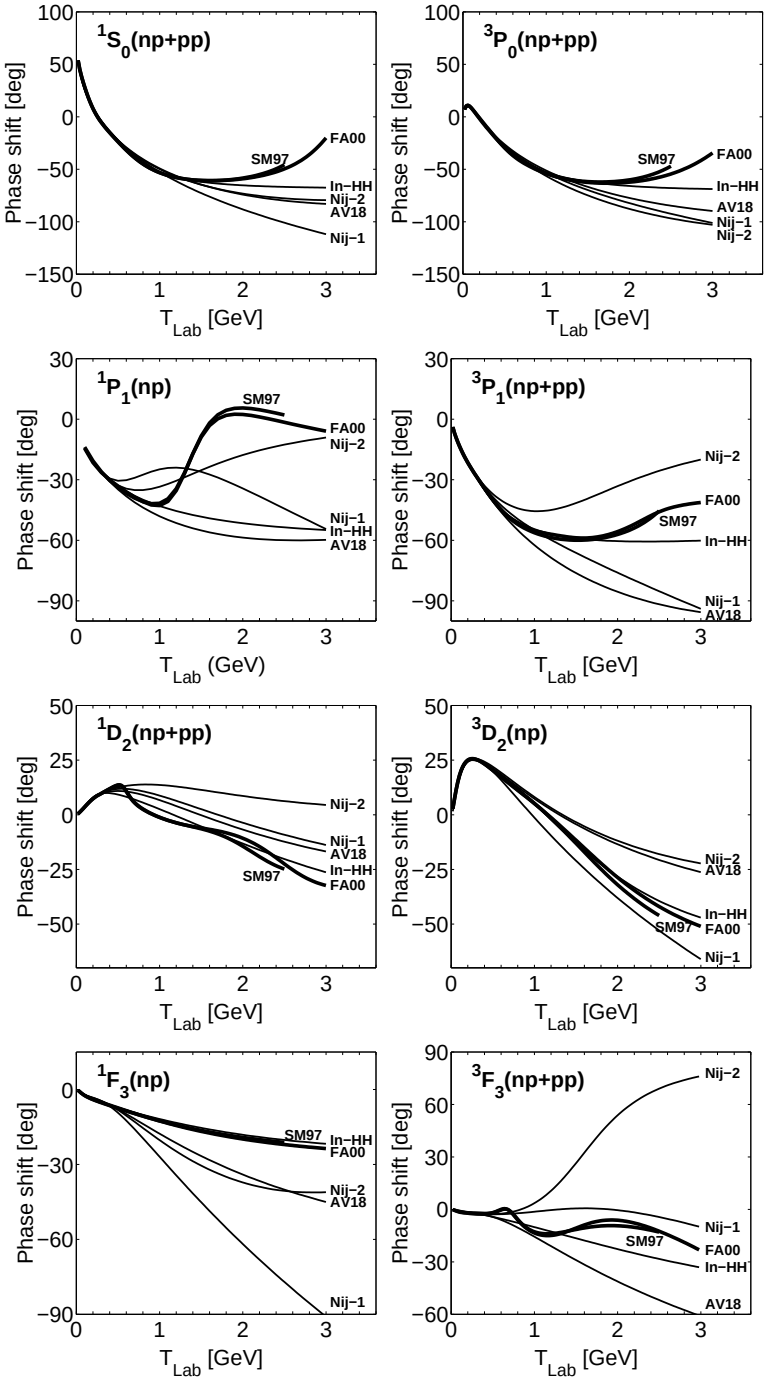

Figure 1: Single channel phase shifts for SM97 $T_{Lab} < 2.5$ GeV), FA00 $T_{Lab} < 3$ GeV, and reference phase shifts using inversion (In-HH), Nijmegen (Nij-1, Nij-2) and Argonne (AV18) potentials.

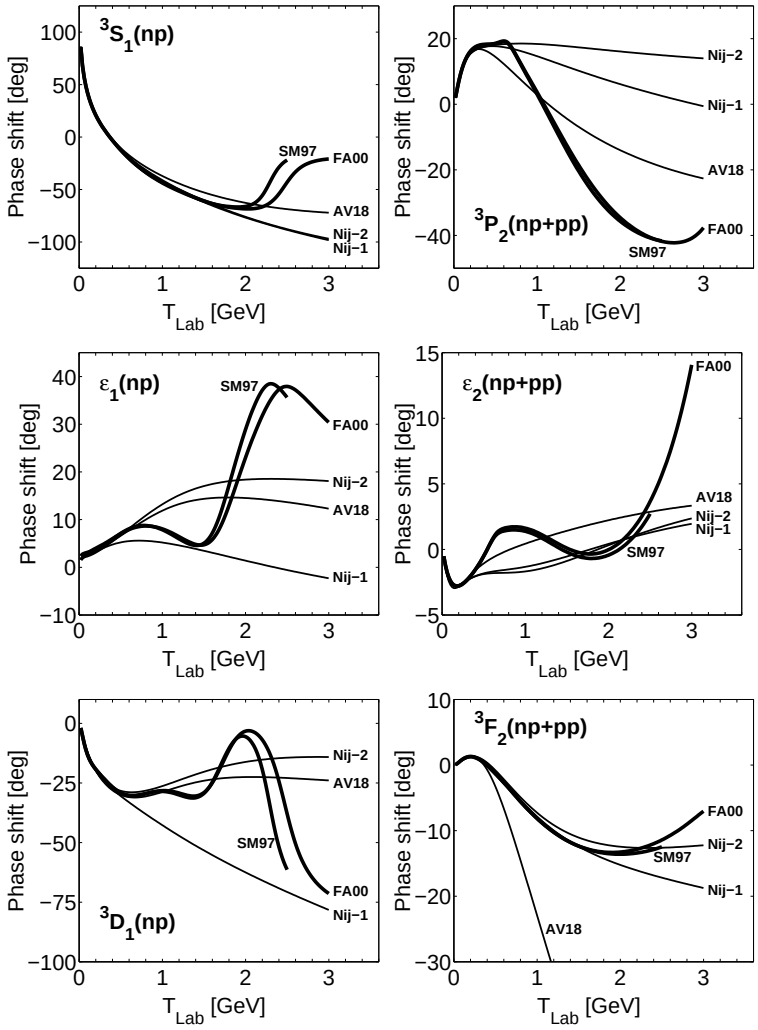

Figure 2: Coupled channel phase shifts for SM97 $T_{Lab} < 2.5$ GeV, FA00 $T_{Lab} < 3$ GeV, and reference phase shifts using Nijmegen(Nij-1, Nij-2) and Argonne (AV18) potentials.

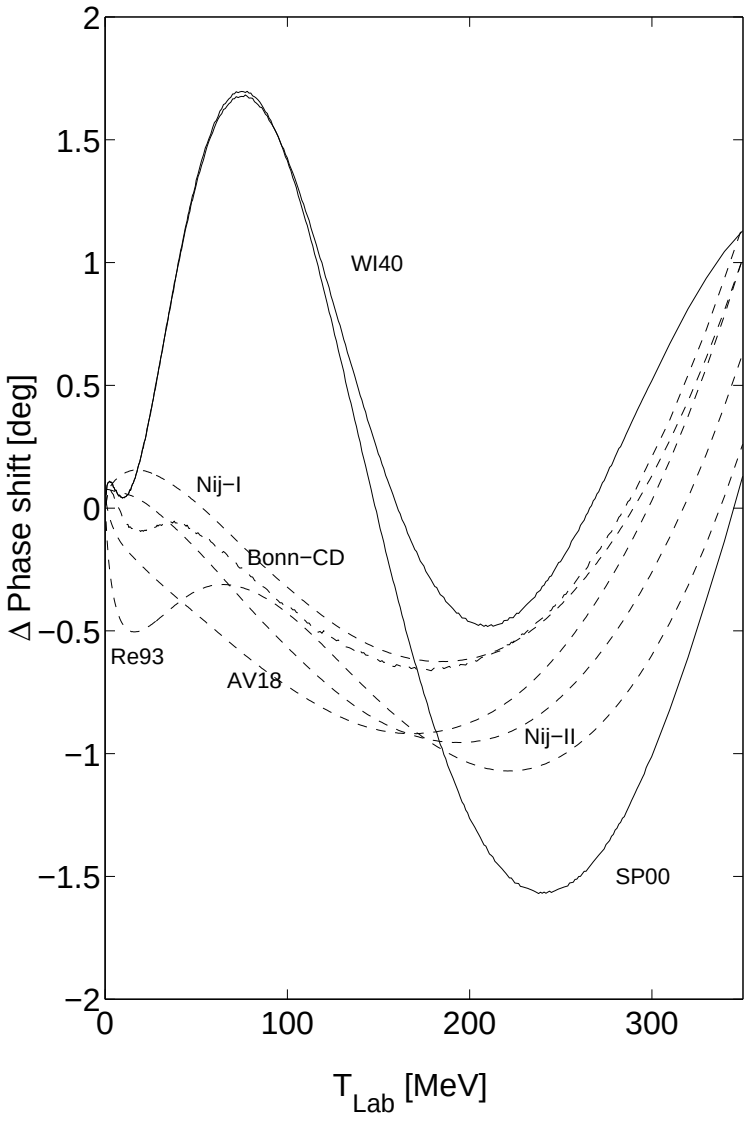

Figure 3: $np\ ^1S_0$ phase shift differences with respect to Nijmegen PWA93.

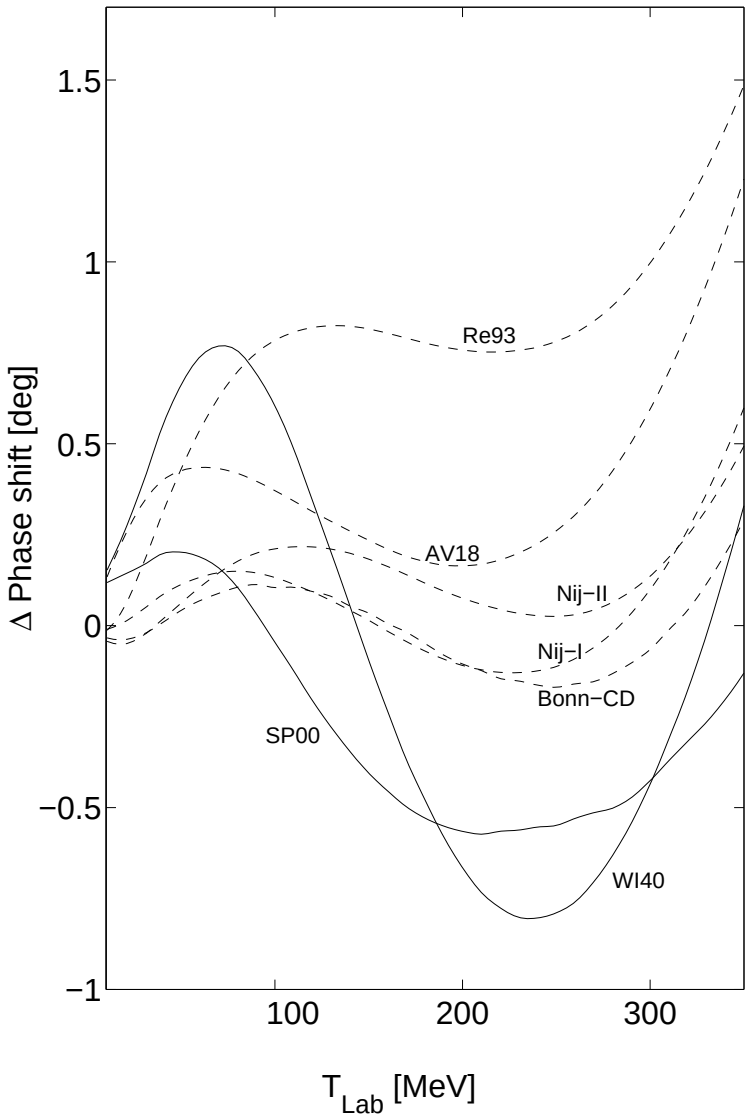

Figure 4: $np\ ^3P_0$ phase shift differences with respect to Nijmegen PWA93.

It is apropos to make a brief remark on the long range character of the NN potential which theoretically is identified with OPEP. In the phase shift analysis PWA93 by the Nijmegen group and in that of Bonn-CD-2000 of Machleidt, such character is enforced. Indeed that precise character re-emerges when either of those phase shift functions are used as input to a Gel'fand–Levitan–Marchenko inversion. On the other hand, the VPI/GWU group makes no use of OPEP in any of their solutions. Exactly the same quantum inversion of the SM94 solution does not give OPEP except on average which might be interpreted as signaling the importance of nonlocality[26].

Despite limitations as discussed above, the OBEP remain the best motivated potential models for low energy scattering. They do yield high quality fits to the phase shifts in that domain. Such is useful for us in our quest to interpret data with increasing energy. In Fig. 5 we show an interaction scheme in terms of radial separation that is suitable for low energy

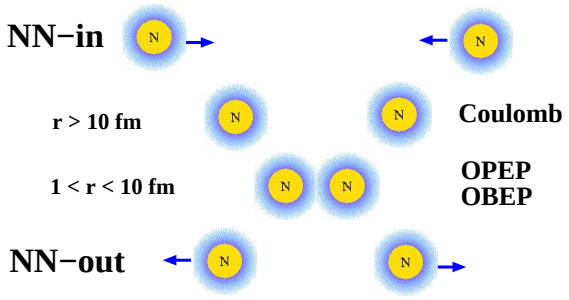

Figure 5: Interaction scheme for low energy scattering, $0 < T_{Lab} < 300$ MeV

scattering. This scheme is supported by potentials determined by inversion which reproduce the low energy phase shifts used as input to an accuracy $|\delta(exp.) - \delta(rat.)| < 0.25$ degrees. Such inversion potentials have been made also to follow closely the SP00 real phase shifts to 3 GeV and these are shown in Fig. 6. They possess a long range Yukawa tail, a medium range attraction ∼1-2 fm and a strong short range repulsion with an onset at 1 fm. These potentials are energy independent so that the long and medium range potential properties diminish in importance for kinetic energies above 500 MeV. For projectiles with $T_{Lab} > 1.5$ GeV essentially only the repulsive core of these potentials remains of significance for scattering. Thus inversion potentials have also been obtained with the SP00 real phase shifts to 3 GeV using $w_{Low} = 0.1$ for $T_{Lab} < 1.2$ GeV and $w_{High} = 1$ for higher energies, to emphasize the high energy data and fix more stringently the short range (< 1 fm) character of the deduced interaction. The short range properties of inversion potentials so found are displayed in Fig. 7. Clearly, the $^1S_0$ and $^3P_{0,1}$ inversion potentials based upon SP00 real phase shifts which extend to 3 GeV are soft core interactions. We neglected in this analyses the np $^1P_1$ channel due to the limited data set for $T_{Lab} < 1.2$ GeV. The higher partial waves are strongly screened by the centripetal barrier and so also are not considered here. The core strengths of these $^1S_0$ and $^3P_{0,1}$ potentials reach a shoulder and maximum with a typical value ~ 1 GeV at a radius of 0.3 to 0.4 fm. It is worth noting that the shoulder/maximum aspect of the core is a result of flat minima between 1.5

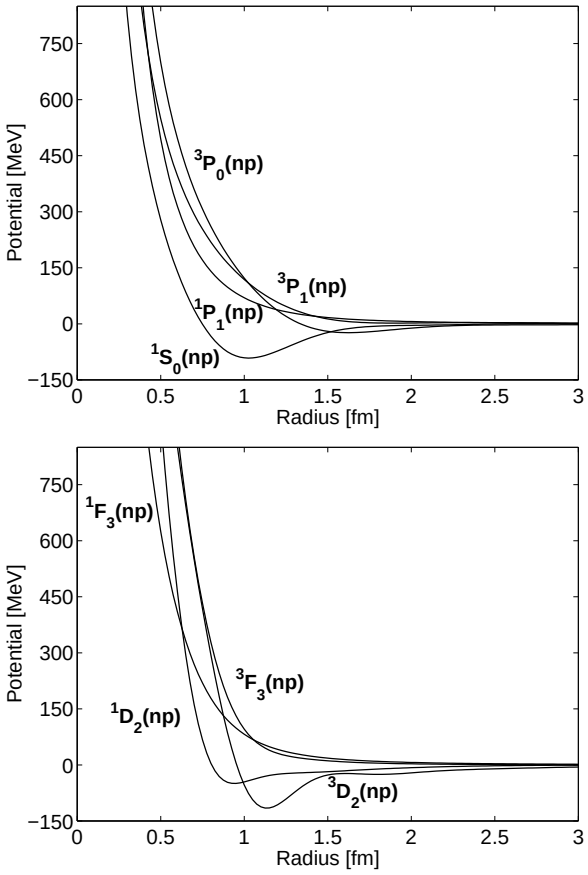

Figure 6: Nucleon-nucleon inversion potentials using SP00 phases

and 2 GeV in the $^1S_0$ and $^3P_{0,1}$ SP00 phase shift functions. For higher partial waves, phase shift minima lie beyond 3 GeV. As the experimental phase shifts are limited to 3 GeV we have confidence in the specified inversion potentials only to about 0.25 fm. The shorter distance values reflect only our extrapolation of these phase shifts being $\lim_{k\to\infty}\delta(k) \sim 1/k$.

Above 300 MeV reaction channels open and the elastic channel S-matrix no longer is unitary. In Fig. 8 we show the gradual increase of the open channels in NN scattering which includes resonances as well as single and multiple production thresholds. Only the $\Delta(1232)$ resonance has a low energy threshold and a relative small width of 120 MeV. Therefore it is the only resonance we expect to be obviously visible in the energy variation of the elastic scattering phase shifts. In particular one notices typical variations in the $^1D_2$, $^3F_3$, and $^3PF_2$ channels. Otherwise the phase shifts to 3 GeV are very smooth slowly changing functions of energy in all channels. Such is a condition for the suitability of a potential model of scattering governed by *quasi* macroscopic geometric entities. In nucleon-nucleus (NA) scattering, entities of that ilk are epitomized by the parameters of Woods–Saxon potentials. For the NN case, we have

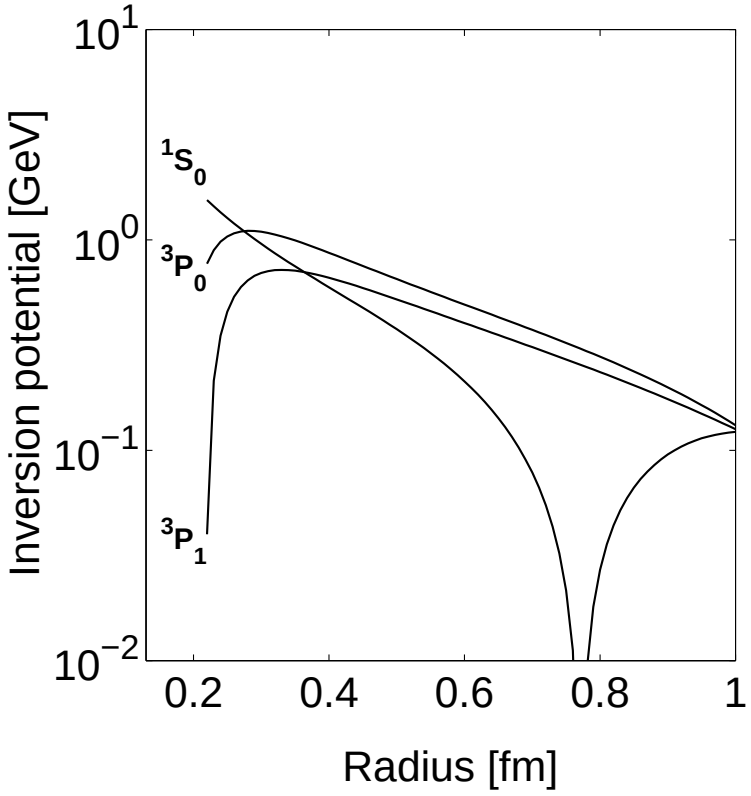

Figure 7: np $^1S_0$ and $^3P_{0,1}$ inversion potentials using SP00 real phase shift solution to 3 GeV.

used previously [16] a local Gaussian in this same manner, noticing therefrom spin-isospin coupling effects more substantial than found with NA scattering. It is also worth noting that the absorption in those NN optical potentials for this energy range were not at the geometric limit of a fully absorptive disc. Together with the strong spin-isospin coupling, this property infers optical potentials that are strongly channel dependent in contrast to the NA case for which assumed central and spin-orbit potentials are partial wave independent.

The plethora of reaction channels that open to 3 GeV, and the requirement of an NN optical potential prescription discussed above, mean that it is an interesting but very challenging task for any microscopic model to uniquely link QCD substructures to NN scattering phase shift functions in analogy to that successful prescription by which NA optical potentials have been determined by folding effective NN interactions with nuclear density matrix elements[18]. Given the success of optical models for NA scattering and as the distorted wave Born approximation (DWBA) is well known and successful in nuclear, atomic and molecular physics to study inelastic reactions, it is intriguing to conjecture use of the DWBA to analyze inelastic reaction channels of NN induced reactions.

In the spirit of visualization of NN scattering shown in Fig. 5, we now include the importance

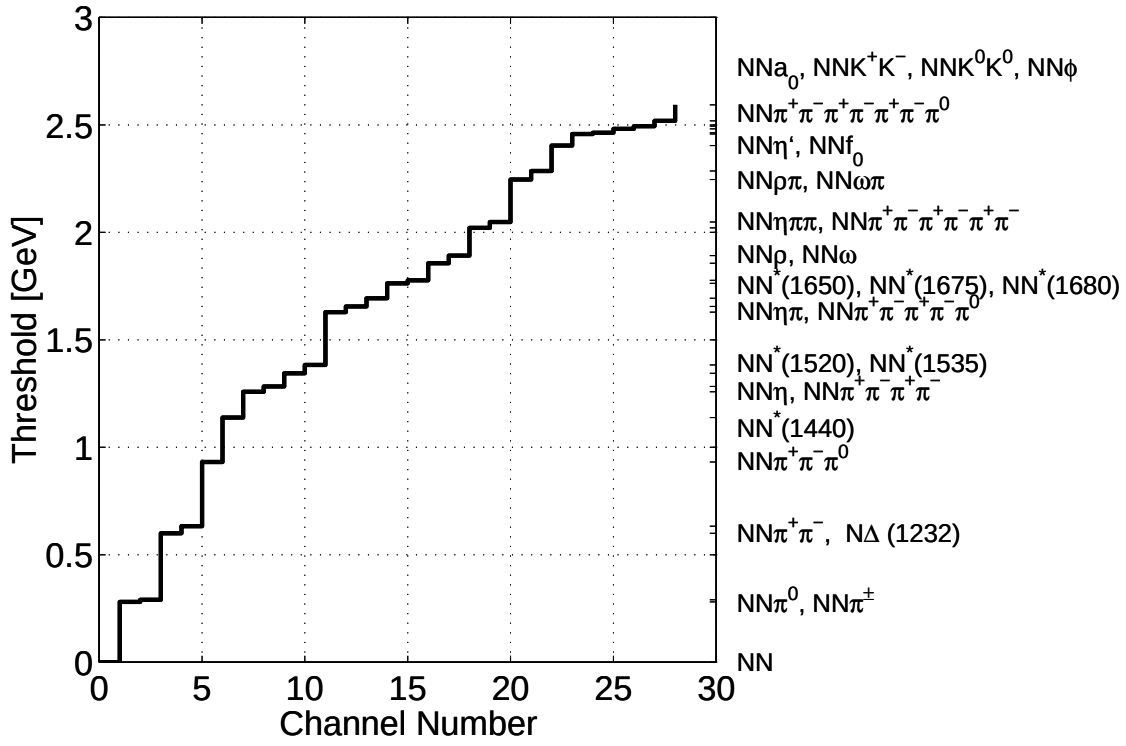

Figure 8: Thresholds for production processes in NN scattering.

of the reactive and resonant content pictorially in Fig. 9. This we consider relevant for $0.3 < T_{Lab} < 2$ GeV. The upper limit is significant here as we discuss later, but for now it suffices that the potential shoulder and maximum seen in Fig. 7 are $\sim$1 GeV. Now we identify some specifics in the $0.5 < r < 1$ fm range. We conjecture that the two colliding hadrons are retained in hadronic states throughout the process. We allow one of the two nucleons to be excited, say into a $\Delta(1232)$, while the other remains in the ground state. The excitation may be exchanged between the two hadrons as well, and both nucleons may be excited to an intermediate resonant state. The production of mesons then can only occur from one or both of the two separate QCD entities. The essential feature is that in the energy range, the predominant scattering processes are those retaining identifiable hadronic entities. Within an optical potential representation, attendant flux loss equates to a diffuse absorption extending radially to 3 fm and possibly more. The bulk of such absorption however lies significantly within 1 fm.

It requires 2 GeV and more for the two nucleons to surpass the core potential barrier and to fuse into a compound system. This is visualized with the scattering sequences shown in Fig. 10. An objective of our optical model studies is to substantiate this conjecture of fusion and fission of resultant compound dibaryonic systems dominating the scattering for this energy regime.

To describe this developing system for 300 MeV $< T_{Lab} <$ 3 GeV we will use Feshbach theory to specify the optical potential[31]. An important feature of that theory is the projection

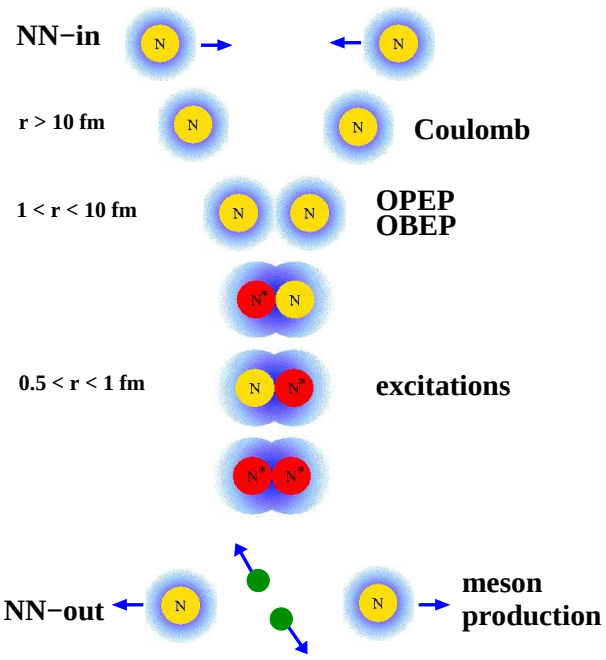

Figure 9: Interaction scheme for medium energy scattering, $0.3 < T_{Lab} < 2$ GeV.

operator formalism with P and Q subspaces, which divide the complete Hilbert space $(P+Q) = 1$, into the elastic scattering channel, the P space, and all inelastic and reaction channels which are contained in Q space. This theory then assumes a hierarchy of complication in Q space of which doorway states are the simplest. Doorway states are characterized to be the only means to leave and to return to the elastic channel. Each doorway state in this approach infers a complex and separable component in the optical potential with an energy dependent strength. If a very large number of doorway states contribute, the effect equates to a local potential operator. This was the basis of our previous study [16].

2.1 Formal Potential Model

It is generally accepted that a valid covariant description of NN scattering formally is given by the Bethe–Salpeter equation

$$\mathcal{M} = \mathcal{V} + \mathcal{V}\mathcal{G}\mathcal{M} \ , \tag{15}$$

where $\mathcal{M}$ are invariant amplitudes that are based upon all connected two particle irreducible diagrams. This equation serves generally as an ansatz for approximations. Of those, the three dimensional reductions are of great use which allow the definition of a potential [32, 33]. In particular, the Blankenbecler–Sugar reduction [32] gives an equation very often used for applications with NN scattering [20, 34]. This reduction is obtained from Eq. (15), which in

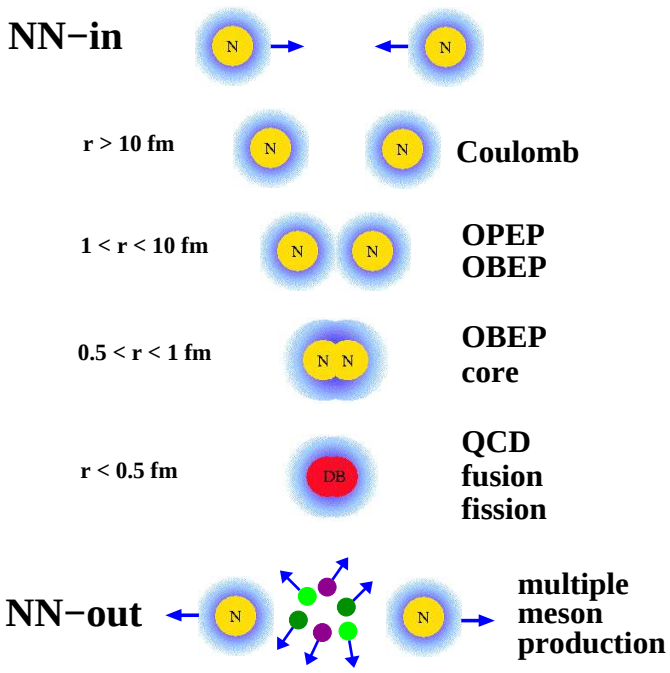

Figure 10: Interaction scheme for high energy scattering, $T_{Lab} > 2$ GeV

terms of four-momenta is

$$\mathcal{M}(q',q;P) = \mathcal{V}(q',q;P) + \int d^4k\ \mathcal{V}(q',k;P)\ \mathcal{G}(k;P)\ \mathcal{M}(k,q;P), \tag{16}$$

where the propagator

$$\mathcal{G}(k;P) = \frac{i}{(2\pi)^4}\left[\frac{\frac{1}{2}\not{P}+\not{k}+M}{(\frac{1}{2}P+k)^2-M^2+i\varepsilon}\right]_{(1)}\left[\frac{\frac{1}{2}\not{P}-\not{k}+M}{(\frac{1}{2}P-k)^2-M^2+i\varepsilon}\right]_{(2)}. \tag{17}$$

The subscripts refer to nucleon (1) and (2) respectively. In the CM system $P = (\sqrt{s}, 0)$, which is just the total energy $E = \sqrt{s}$. In particular, the Blankenbecler–Sugar reduction of the propagator $\mathcal{G}$ uses the covariant form

$$\mathcal{G}_{\rm BS}(k,s) = -\frac{\delta(k_0)}{(2\pi)^3}\frac{M^2}{E_k}\frac{\Lambda^+_{(1)}(\mathbf{k})\Lambda^+_{(2)}(-\mathbf{k})}{\frac{1}{4}s - E_k^2 + i\varepsilon}\ , \tag{18}$$

with positive energy projectors

$$\Lambda^+_{(i)}(\mathbf{k}) = \left(\frac{\gamma^0 E_k - \vec{\gamma}\cdot\mathbf{k} + M}{2M}\right)_{(i)}. \tag{19}$$

The amplitudes are now expressed with the reduced terms and they satisfy a three-dimensional equation

$$\mathcal{M}(\mathbf{q}',\mathbf{q}) = \mathcal{V}(\mathbf{q}',\mathbf{q}) + \int \frac{d^3k}{(2\pi)^3}\mathcal{V}(\mathbf{q}',\mathbf{k})\frac{M^2}{E_k}\frac{\Lambda^+_{(1)}(\mathbf{k})\Lambda^+_{(2)}(-\mathbf{k})}{\mathbf{q}^2-\mathbf{k}^2+i\varepsilon}\mathcal{M}(\mathbf{k},\mathbf{q}). \tag{20}$$

Taking matrix elements with only positive energy spinors, an equation with minimum relativity results for the NN t-matrix, namely

$$\mathcal{T}(\mathbf{q}',\mathbf{q}) = \mathcal{V}(\mathbf{q}',\mathbf{q}) + \int \frac{d^3k}{(2\pi)^3}\mathcal{V}(\mathbf{q}',\mathbf{k})\frac{M^2}{E_k}\frac{1}{\mathbf{q}^2-\mathbf{k}^2+i\varepsilon}\mathcal{T}(\mathbf{k},\mathbf{q}). \tag{21}$$

Using the substitutions

$$T(\mathbf{q}',\mathbf{q}) = \left(\frac{M}{E_{q'}}\right)^{\frac{1}{2}}\mathcal{T}(\mathbf{q}',\mathbf{q})\left(\frac{M}{E_q}\right)^{\frac{1}{2}} \tag{22}$$

and

$$V(\mathbf{q}',\mathbf{q}) = \left(\frac{M}{E_{q'}}\right)^{\frac{1}{2}}\mathcal{V}(\mathbf{q}',\mathbf{q})\left(\frac{M}{E_q}\right)^{\frac{1}{2}}, \tag{23}$$

a simplified form of the t-matrix is obtained. It is the familiar Lippmann–Schwinger equation

$$T(\mathbf{q}',\mathbf{q}) = V(\mathbf{q}',\mathbf{q}) + \int \frac{d^3k}{(2\pi)^3}V(\mathbf{q}',\mathbf{k})\frac{M}{\mathbf{q}^2-\mathbf{k}^2+i\varepsilon}T(\mathbf{k},\mathbf{q})\ . \tag{24}$$

Of use is an equivalent Lippmann–Schwinger equation for the wave function. Formally, this equivalence is proven with the Møller distortion operator which relates the free wave function with the scattered wave and uses the relation between scattering amplitude and potential, $T^{(\pm)}\Phi = V\Omega^{(\pm)}\Phi$. Finally, we use the equivalence between the Lippmann–Schwinger integral equation and the Schrödinger equation so that

$$\left(-\Delta + \frac{M}{\hbar^2}V(\mathbf{r}) - k^2\right)\psi(\mathbf{r},\mathbf{k}) = \mathbf{0}. \tag{25}$$

When we identify the potential scale M with the two particle reduced mass

$$M = 2\mu = 2\frac{m_1 m_2}{m_1+m_2} \tag{26}$$

we guarantee consistency with the low energy limit of the Schrödinger equation and use, therein, of NN OBE reference potentials. However, a careful and consistent treatment of the M/E factors in Eqs. (22) and (23) is necessary whenever it is important to take relativity into account. Minimal relativity enters in the calculation of k^2 by

$$s = (m_1+m_2)^2 + 2m_2T_{Lab} = \left(\sqrt{k^2+m_1^2}+\sqrt{k^2+m_2^2}\right)^2\ , \tag{27}$$

where

$$k^2 = \frac{m_2^2(T_{Lab}^2+2m_1T_{Lab})}{(m_1+m_2)^2+2m_2T_{Lab}}\ . \tag{28}$$

For equal masses this reduces to $k^2 = s/4 - m^2$.

3 An algorithm for the optical and boundary condition models

We distinguish between three Hamiltonians. They are the *reference* Hamiltonian H_0, a projected Hamiltonian H_{PP}, and a full optical model Hamiltonian $\mathcal{H}$. The first of these, the *reference* Hamiltonian $H_0 := T + V_0$, invokes a given potential V_0 for which one can find Schrödinger equation reference solutions. The physical outgoing solutions $\psi_0 := \psi_0^+(\mathbf{r}, \mathbf{k}, E)$ of H_0 we suppose gives a unitary S-matrix. We assume further that this Hamiltonian is completely specified such that evaluation of any quantity, wave function, S-matrix, K-matrix *etc.* is facilitated. The Feshbach projection operator formalism[31] is used to give the *projected* Hamiltonian, $PH_0P = H_{PP}$, derived from H_0. We presuppose completeness, $P + Q = 1$, and a finite rank representation of the Q space

$$Q := \sum_{i=1}^{N} |\Phi_i >< \Phi_i| = \sum_{i=1}^{N} |i >< i|, \tag{29}$$

with the Q space basis functions $|\Phi_i >$ interpreted as doorway states. With these doorway states we make the link between the QCD and the hadronic sectors; the latter encompassing nucleons, mesons and other free particles. Thus we will assume that meson creation/annihilation occurs only in the highly nonlinear QCD sector so that Q space wave functions are projections of such processes onto hadronic particle coordinates. The third of our Hamiltonians, the *full optical model* Hamiltonian, comprises the reference Hamiltonian H_0 and the proper optical model potential $\mathcal{V}$. That potential is complex and nonlocal, *viz.* separable of finite rank, $\mathcal{H} := T + V_0 + \mathcal{V}(r, r'; lsj, E)$. Separable potentials are popular representations of NN potentials which are designed to serve quite a wide range of purposes [35].

The Schrödinger equation specified with $\mathcal{H}$ has regular physical solutions $\Psi^+ := \Psi^+(\mathbf{r}, \mathbf{k}, E)$ whose asymptotic boundary conditions we deem to match with the *experimental* elastic channel S-matrix. Specifically, for these experimental S-matrices we have used the continuous solutions SP00 from VPI/GWU [28]. The reference potential V_0 and separable potential form factors are to be specified in detail with any application.

3.1 Towards a full optical potential model

To obtain the optical potential on the basis of a given reference potential, we express first the solutions of the projected Hamiltonian in terms of the reference Hamiltonian and the *a priori* defined Q space projector. The Schrödinger equation $(E - H_0)|\psi_0 >= 0$ and its solutions are used to express the solutions of $(E - H_{PP})|\psi_P >= 0$. The latter is equivalent to the Schrödinger equation

$$(E - H_{PP} - H_{QP} - H_{PQ} - H_{QQ})|\psi_P >= -H_{QP}|\psi_P > \tag{30}$$

and the Lippmann–Schwinger equation

$$\begin{aligned} |\psi_P> &= |\psi_0> - \frac{1}{(E^+ - H_0)} H_{QP} |\psi_P> \\ &= |\psi_0> - \sum_j G^+ |j><j| H_{QP} |\psi_P> . \end{aligned} \tag{31}$$

These equations are still very general and do not depend upon a specific representation. However, in the following we assume a partial wave expansion in terms of spherical harmonics, spin and isospin state vectors and radial functions. The following equations are identified as radial equations with the set of quantum numbers suppressed.

Projector orthogonality $PQ = QP = 0$ implies that

$$0 = <i|\psi_P> = <i|\psi_0> - <i|G^+ H_{QP}|\psi_P>, \tag{32}$$

and thus

$$<j|H_{QP}|\psi_P> = \sum_i^N \{<\Phi|G^+|\Phi>\}^{-1}_{ji} <i|\psi_0> . \tag{33}$$

The solutions of Eq. (31) can be written in terms of $|\psi_0>$ as

$$|\psi_P> = |\psi_0> - \sum_{ij}^N G^+ |i> \{<\Phi|G^+|\Phi>\}^{-1}_{ij} <j|\psi_0> = |\psi_0> - \sum_{ij}^N G^+ \Lambda_{ij} |\psi_0>, \tag{34}$$

wherein one can identify a separable potential

$$|i> \{<\Phi|G^+|\Phi>\}^{-1}_{ij} <j| = |i> \lambda_{ij} <j| =: \Lambda_{ij}(r, r') \tag{35}$$

Note then that definition of Q space gives a specification of the separable strengths $\lambda_{ij}(lsj, E)$ that is unique. The resultant Eq. (34) has the form of a first order Born approximation but in fact it is an exact result.

To proceed, we initially abandon the exactitude of Eq. (34) and require the strength matrix,

$$\lambda_{ij} = \{<\Phi|G^+|\Phi>\}^{-1}_{ij}, \tag{36}$$

to be constrained asymptotically by the experimental S-matrix of the full Hamiltonian Schrödinger equation, *i.e.* asymptotically we induce $|\psi_P> = |\Psi_{\mathcal{H}}>$. This implies that complex optical model strengths λ_{ij} emerge as a result of matching to Riccati-Hankel functions and non unitary S-matrices with

$$|\Psi_{\mathcal{H}}> = |\psi_P> \sim \frac{1}{2i} \left[-h^-(rk) + h^+(rk) S(k) \right] . \tag{37}$$

The strengths λ_{ij} then can be simply determined from the linear system of equations

$$\frac{1}{2i} h^+(Rk) \left[S(k) - S_0(k) \right] = \sum_{ij} G^+ |i> \lambda_{ij} <j|\psi_0^+> . \tag{38}$$

To reinforce a Lippmann–Schwinger equation, with the experimental S-matrix as boundary condition or equivalently with strengths λ_{ij} from Eq. (38), a transformation of the separable potential Eq. (35) is made. This is achieved with

$$\mathcal{V}(r,r') := \Lambda \frac{1}{(1-G^+\Lambda)}, \tag{39}$$

which contains the separable potentials as defined with Eq. (35) but whose strengths now are solutions of Eq. (38). As the transformation Eq. (39) contains integration of orthonormal functions, only strengths are altered. Using this optical model in the full Hamiltonian, physical solutions are obtained with reference solutions $|\psi_0>$ and Greens function G^+ of the reference Hamiltonian H_0 by means of the Lippmann–Schwinger equation

$$|\Psi_{\mathcal{H}}>= |\psi_0> + G^+\mathcal{V}|\Psi_{\mathcal{H}}> . \tag{40}$$

3.2 Technical details

The partial wave radial wave functions of the reference potential satisfy equations

$$u''_\alpha(r,k) = \left[\frac{\ell(\ell+1)}{r^2} + \frac{2\mu}{\hbar^2}\frac{V_a(r)}{1+2V_b(r)} - \left(\frac{V'_b(r)}{1+2V_b(r)}\right)^2 - \frac{k^2}{1+2V_b(r)}\right] u_\alpha(r,k), \tag{41}$$

wherein we identify the complete set of quantum numbers by the subscript α. These equations we have solved numerically for uncoupled and coupled channels using a Numerov method. The potentials V_a, V_b, V'_b are dependent on the quantum numbers (ℓ, s, j) and are taken from the Paris, Nijmegen, Argonne, and inversion r-space potentials as one wishes. The Paris and Nijmegen-I are momentum dependent potentials with $V_b \neq 0$, while the Nijmegen-II, Reid93, AV18, and inversion potentials all have $V_b = 0$. The physical solutions are matched asymptotically to Riccati-Hankel functions

$$u^+_\alpha(r,k) \sim \frac{1}{2i}\left[-h^-_\alpha(rk) + h^+_\alpha(rk)S^0_\alpha(k)\right] \tag{42}$$

and normalized by

$$\psi^+_\alpha(r,k) = \frac{u^+_\alpha(r,k)}{\sqrt{1+2V_b(r)}}. \tag{43}$$

The irregular outgoing wave Jost solutions

$$\mathcal{J}^+_\alpha(r,k) \sim h^+_\alpha(rk) \tag{44}$$

are calculated in the same way as the physical ones and they define the reference potential Green functions by

$$G^+_\alpha(r,r',k) = \begin{cases} -\left(2\mu/\hbar^2\right)\dfrac{1}{k}\psi^+_\alpha(r,k)\mathcal{J}^{+T}_\alpha(r',k), & r<r' \\ -\left(2\mu/\hbar^2\right)\dfrac{1}{k}\mathcal{J}^+_\alpha(r,k)\psi^{+T}_\alpha(r',k), & r>r', \end{cases} \tag{45}$$

where the transpose matrix is signaled by the superscript T. At the asymptotic matching radius R

$$\Psi_\alpha^+(R,k) = \psi_\alpha^+(R,k) + \int_0^\infty G_\alpha^+(R,r_1,k)\Phi_\alpha(r_1)dr_1\lambda_\alpha(k)\int_0^\infty \Phi_\alpha(r_2)\psi_\alpha^+(r_2,k)dr_2, \tag{46}$$

and taking the difference between the reference and full S-matrix, this reduces to

$$\begin{aligned}\Psi_\alpha^+(R,k) - \psi_\alpha^+(R,k) &= \frac{1}{2i}h_\alpha^+(Rk)\left[S_\alpha(k) - S_\alpha^0(k)\right] \\ &= \int_0^\infty G_\alpha^+(R,r_1,k)\Phi_\alpha(r_1)dr_1\lambda_\alpha(k)\int_0^\infty \Phi_\alpha(r_2)\psi_\alpha^+(r_2,k)dr_2. \end{aligned}\tag{47}$$

A linear expression for the potential strength $\lambda_\alpha(k)$ results. The strengths are transformed by Eq. (39) to give final separable potential strengths

$$\sigma_\alpha(k) = \left(1 - \lambda_\alpha(k)\int_0^\infty\int_0^\infty \Phi_\alpha(r_1)G_\alpha^+(r_1,r_2,k)\Phi_\alpha(r_2)\,dr_1\,dr_2\right)^{-1}\lambda_\alpha(k). \tag{48}$$

These strengths $\sigma_\alpha(k)$ define the proper optical model of Eq. (40), given for the more general coupled channel and rank ≤ 3 separable potentials, to be

$$\mathcal{V}(r,r') = |\Phi_\alpha > \sigma_\alpha < \Phi_\alpha| = \frac{2\mu}{\hbar^2}\Phi_\alpha\mathcal{W}_\alpha\Phi_\alpha^T \tag{49}$$

where

$$\Phi_\alpha := \left\{ \begin{array}{cccccc} \Phi^1_{j-1/2}(r) & \Phi^2_{j-1/2}(r) & \Phi^3_{j-1/2}(r) & 0 & 0 & 0 \\ 0 & 0 & 0 & \Phi^1_{j+1/2}(r) & \Phi^2_{j+1/2}(r) & \Phi^3_{j+1/2}(r) \end{array} \right\}, \tag{50}$$

and the symmetric strength matrices are

$$\mathcal{W}_\alpha(k) := \mathrm{Re}W_{i,j} + i\mathrm{Im}W_{i,j} = (\hbar^2/2\mu)\;\sigma_\alpha(k),\ \text{for } i,j = 1\cdots 6. \tag{51}$$

For single channel and rank one potentials, this representation is obviously reduced.

There are several options one may consider for the separable potential form factors $\Phi_\alpha(r)$. First, any finite rank potential may be chosen with the strengths $\lambda_\alpha(k)$ determined from data at several energies around a mean energy. In practice, using a rank > 1 option has been successful for single channels but inherent lack of energy dependence for coupled channels strongly favors restricting potentials to be of rank one. Next is the choice of radial form factors. As rank one potential form factors we have used a.) normalized harmonic oscillator radial wave functions $\Phi_\alpha = \Phi_\ell(r,\hbar\omega)$, b.) normalized Gaussian functions $\Phi_\alpha = N_0\exp -(r-r_0)^2/a_0^2$ with r_0 and a_0 being parameters, c.) a normalized edge function $\Phi_\alpha(r_0) = 1/2h, \Phi_\alpha(r_0 \pm h) = 1/4h$ and $\Phi_\alpha(r,\alpha) = 0$ otherwise, and d.) a boundary condition model realized by $\Phi_\alpha(r_0) = 1/h$ and $\Phi_\alpha(r) = 0$ otherwise. The last option is suitable for a sudden transition from the hadronic

domain into the QCD domain and back. Of course these are but examples and others may be inspired by more explicit considerations of QCD.

Solutions of the full problem Lippmann–Schwinger equation, Eq. (40), have been generated with reference potential solutions and Green functions as per Eq. (45) and with separable potentials whose strengths $\sigma_\alpha(k)$ are given by Eq. (48). These solutions are readily found from systems of linear equations, for single and coupled channels, using a trapezoidal integration rule for Eq. (40) recast as

$$\Psi^+_\alpha(r) = \psi^+_\alpha(r) + \int_0^\infty G^+_\alpha(r,r_1)\Phi_\alpha(r_1)dr_1\mathcal{W}_\alpha(k)\ \int_0^\infty \Phi_\alpha(r_2)\Psi^+_\alpha(r_2)\,dr_2\ . \tag{52}$$

However there is a faster method by which solutions Eq. (46) as well as half off-shell wave function solutions and t-matrices can be found. This we consider next.

3.3 Evaluation of the half off-shell t-matrix

The calculation of NA optical potentials for $T_{Lab} < 3$ GeV requires half off-shell NN t-matrices for on-shell k-values $k < 6$ fm^{-1}, and a correspondingly large range of off-shell values. In principle, in applications the off-shell k-values (later identified with q) are needed in integrals from $0 \to \infty$ but a reasonable upper limit is $q = 2k$. A fast and stable method of evaluation of such half off-shell t-matrices, when r-space potentials are chosen, is an extension of the Schrödinger equation as an inhomogeneous differential equation. The method follows that of Van Leeuwen and Reiner [36].

The most general potentials in our study contain momentum dependent, local and separable complex potentials for both single and coupled channels. In particular for the results shown, a rank one separable potential with a radial harmonic oscillator form factor $\Phi_\ell(r,\hbar\omega)$ has been used. The Schrödinger equation then can be cast as

$$\left[\mathcal{M}(r)\frac{d^2}{dr^2} - \mathcal{M}(r)\frac{\ell(\ell+1)}{r^2} - V_a(r) + V_b''(r) + 2V_b'(r)\frac{d}{dr} + k^2\right]\psi_\ell(r,k,q)$$

$$= \Phi_\ell(r)\lambda_\ell(k^2)\int_0^\infty \Phi_\ell(x)\psi_\ell(x,k,q)\,dx + (k^2-q^2)j_\ell(rq), \tag{53}$$

with $\mathcal{M}(r) = (1 + 2\,V_b(r))$. The regular solutions of which not only must vanish at the origin but also asymptotically must match to

$$\lim_{r\to\infty}\psi^{(\pm,0)}_\ell(r,k,q)\mathcal{N}_\ell = j_\ell(rq) + h^{(\pm,0)}_\ell(rk)\frac{q}{k}T^{(\pm,0)}_\ell(k^2,k,q) \tag{54}$$

to determine the half off-shell t-matrix $T^{(\pm,0)}_\ell(k^2,k,q)$ and the normalization $\mathcal{N}_\ell$. Spherical Riccati functions are symbolized by $j_\ell(x)$, $h^\pm_\ell(x)$ and $h^0_\ell(x) = n_\ell(x)$. In the following we suppress the channel subscript ℓ as the expressions hold for single and coupled channels. The on-shell t-matrix gives the S-matrix by the relation

$$S(k) = 1 + 2i\,T^{(+)}(k^2,k,k). \tag{55}$$

To solve for coupled channels ${}^3SD_1$, ${}^3PF_2$, *etc.*, two linear independent regular solutions are calculated and Eqs. (48), (53) and (54) are to be understood as 2×2 matrix equations.

The regular solutions are readily found numerically as follows. First, a regular solution of the reference potential Schrödinger equation

$$f_0''(r,k) - V(r) f_0(r,k) + k^2 f_0(r,k) = 0 \tag{56}$$

is calculated. Therein $V(r)$ implies all the local potential terms including the centripetal barrier. Then a regular solution of the full potential Schrödinger equation with the reference potential $V(r)$ and separable potential,

$$f_1''(r,k) - V(r) f_1(r,k) + k^2 f_1(r,k) = \Phi(r)\sigma(k) < \Phi | f_1 >, \tag{57}$$

is obtained from a particular solution of

$$g_1''(r,k) - V(r) g_1(r,k) + k^2 g_1(r,k) = \Phi(r)\sigma(k)\mathcal{F}, \tag{58}$$

where we use $\mathcal{F} =< \Phi | f_0 >$, and $f_1(r,k) = f_0(r,k)\mathcal{A} + g_1(r,k)$. The factor (matrix) $\mathcal{A}$ is determined from

$$< \Phi | f_1 > = < \Phi | f_0 > \mathcal{A} + < \Phi | g_1 > \tag{59}$$

and

$$\mathcal{A} = 1 - \mathcal{F}^{-1} < \Phi | g_1 > . \tag{60}$$

Finally the regular solution $f_1(r,k)$ can be multiplied with any complex number (matrix) to be a general regular solution of Eq. (57).

The half off-shell t-matrix is related to the regular half off-shell wave function $\psi(r,k,q)$, which satisfies the inhomogeneous Schrödinger equation

$$\left[\frac{d^2}{dr^2} - V(r) + k^2\right] \psi(r,k,q) = \Phi(r)\sigma(k) < \Phi | \psi > + (k^2 - q^2) j(rq). \tag{61}$$

Asymptotically this wave function is

$$\psi^{(\pm,0)}(r,k,q) \sim j(rq) + h^{(\pm,0)}(rk)\frac{q}{k} T^{(\pm,0)}(k^2,k,q). \tag{62}$$

A general regular solution of Eq. (57) and a particular regular inhomogeneous solution of Eq. (55) then is needed to satisfy the boundary conditions given in Eq. (62). A particular solution of Eq. (61) is obtained in two steps. First, with

$$\mathcal{F} =< \Phi | g_2 > = < \Phi | f_1 > = < \Phi | f_0 >, \tag{63}$$

a particular solution is given by

$$f_2(r,k,q) = f_1(r,k)\mathcal{B} + g_2(r,k,q), \tag{64}$$

where $\mathcal{B}$ is determined from

$$\mathcal{B} = 1 - \mathcal{F}^{-1} < \Phi | g_2 > . \tag{65}$$

The off-shell wave function matches asymptotically as

$$\psi^{(\pm,0)}(r,k,q) = f_1(r,k)\mathcal{N} + f_2(r,k,q) \sim j(rq) + h^{(\pm,0)}(rk)\frac{q}{k}T(k^2,k,q). \tag{66}$$

The normalization $\mathcal{N}$ and t-matrix $T^{(\pm,0)}(k^2,k,q)$ are readily evaluated from the *quasi* Wronskians

$$\begin{aligned} \mathcal{N} &= W^{-1}[h^{(\pm,0)}, f_1]\left(W[j, h^{(\pm,0)}] - W[h^{(\pm,0)}, f_2]\right) \\ \frac{q}{k}T^{(\pm,0)}(k^2,k,q) &= W^{-1}[j, h^{(\pm,0)}]\Big(W[j,f_1]\mathcal{N} + W[j,f_2]\Big). \end{aligned} \tag{67}$$

where we define

$$W[a,b] := \frac{(a_n - a_{n-1})}{h}b_n - a_n\frac{(b_n - b_{n-1})}{h} \tag{68}$$

at two asymptotic radial points r_{n-1} and $r_n = r_{n-1} + h$. The quantities a and b can be either scalars or matrices.

It is very convenient to use the Numerov algorithm to solve Eqs. (56), (58), and (61). But to do so for Eq. (53) requires equations without first derivative terms. The above can be made so by use of a factorization

$$\psi(r,k,q) = f(r,k,q)\mathcal{D}(r), \text{ with } \mathcal{D}(r) = \frac{1}{\sqrt{1 + 2V_b(r)}} \tag{69}$$

The resulting equation for $f(r,k,q)$ is

$$\begin{aligned} f''(r,k,q) = \Bigg[\ell(\ell+1)/r^2 - \mathcal{D}(r)k^2\mathcal{D}(r) + \mathcal{D}(r)V_a(r)\mathcal{D}(r) + \Big(\mathcal{D}(r)V_b'(r)\mathcal{D}(r)\Big)^2\Bigg] f(r,k,q) \\ + \Phi(r)\mathcal{D}(r)\sigma(k) < \mathcal{D}\Phi | f > + (k^2 - q^2)j_\ell(rq)\mathcal{D}(r). \end{aligned} \tag{70}$$

3.4 Numerov Algorithm

The solution of radial Schrödinger equations is certainly not new and generally deserves no mention. Here, we dwell upon the details since we found the specified elements to have a *normal form* of related problems in other fields of physics and engineering which were tested with parallel computing facilities. The Numerov algorithm has been widely used for single and coupled channels Schrödinger equations since it gives sufficient numerical accuracy with minimal operations [37]. The standard form of linear homogeneous or inhomogeneous Schrödinger equations which we have to solve is

$$f_i''(r) = V_{ij}(r)f_j(r) + W_i(r), \tag{71}$$

where $W_i(r) = 0$ for homogeneous equations. The terms $V_{ij}(r)$ and $W_i(r)$ are easily identified in Eq. (70). For single channels the algorithm is

$$f_{n+1} = 2f_n - f_{n-1} + \frac{h^2}{12}\left(u_{n+1} + 10u_n + u_{n-1}\right) \tag{72}$$

or

$$\begin{aligned}\left(1 - \frac{h^2}{12}V_{n+1}\right) f_{n+1} &= \left(2 + \frac{10h^2}{12}V_n\right) f_n - \left(1 - \frac{h^2}{12}V_{n-1}\right) f_{n-1} \\ &+ \frac{h^2}{12}\left(W_{n+1} + 10\,W_n + W_{n-1}\right)\ .\end{aligned} \tag{73}$$

These expressions generalize for coupled channels using standard vector and matrix algebra. A significant reduction of operations is found by using the substitution

$$\xi_n = \left(1 - \frac{h^2}{12}V_n\right) f_n \tag{74}$$

in Eq. (73). It gives

$$\xi_{n+1} = 2\xi_n - \xi_{n-1} + \mathcal{U}_n, \tag{75}$$

and the inhomogeneous equation

$$\xi_{n+1} = 2\xi_n - \xi_{n-1} + \mathcal{U}_n + \frac{h^2}{12}\left(W_{n+1} + 10W_n + W_{n-1}\right), \tag{76}$$

with

$$\mathcal{U}_n = \frac{h^2 V_n}{1 - \frac{h^2}{12}V_n}\xi_n. \tag{77}$$

Back-transformations from $\xi_i \to f_i$ use either of the two possibilities

$$f_i = \xi_i + \frac{1}{12}\mathcal{U}_i, \text{ or } \quad f_i = \frac{\xi_{i+1} + 10\xi_i + \xi_{i-1}}{12}. \tag{78}$$

4 Properties and discussion of the optical model.

A range of optical potentials have been generated using the algorithm developed above. As reference potentials, the Paris, Nijmegen, Argonne, and inversion potentials have been used. For the separable potential form factors, normalized harmonic oscillator functions (HO), $\Phi_\ell(r, \hbar\omega)$, with $200 < \hbar\omega < 900$ MeV have been used. The same $\hbar\omega$ is used for all partial waves however. For single channels all quantum sets with $J \leq 7$ were included while those for $J \leq 6$ were used with the coupled channels. A superposition of several HO functions with radial quantum numbers $n = 1, 2, 3$ was allowed and with data in intervals $T_{Lab} \pm 25$, $T_{Lab} \pm 50$, and $T_{Lab} \pm 100$

MeV, optimal solutions of Eq. (47) found using a least square linear equation routine from a scientific subroutine library (NAG-library). This procedure was used to determine a single $\hbar\omega$ for energies within $0.5 < T_{Lab} < 2$ GeV with an overall low χ^2. That optimal value is $\hbar\omega = 450$ MeV. For higher energies $2 < T_{Lab} < 3$ GeV and low partial waves, this optimal oscillator has bound states embedded in the continuum, but as such they are of no concern in this analysis and so we used $\hbar\omega = 450$ MeV for all energies $0.3 < T_{Lab} < 3$ GeV. With rank one separable potentials, the HO functions (radial quantum number $n = 1$) are

$$\Phi_\ell(r, \hbar\omega) \sim r^{\ell+1} \exp -(r/r_0)^2, \text{ with } r_0 = \sqrt{\frac{2\hbar^2}{\mu\hbar\omega}}, \tag{79}$$

and with $\hbar\omega = 450$ MeV, $r_0 = 0.61$ fm. Then with the separable form fixed, it is trivial to solve Eq. (47) with S-matrix data taken at each energy. In Figs. 11 and 12 we show the full potential model phase shifts that result on solving scattering from the deduced optical potentials. They are *identical* with the SP00 solution.

The strengths $\sigma_\alpha(k)$ of Eq. (48) were determined independently for each given reference potential and the optical potential values of Eq. (51) are shown in Figs. 13 and 14. The lettering in the small sub-figures identify the channel. The curves give the results obtained when the Paris (Pa), Nijmegen-I (N1), Nijmegen-II (N2), Argonne AV18 (Av) and single channel inversion potentials (In) were used as reference potentials. These optical model strengths display two most important features. The first is that they are not insignificant. The reference potentials by themselves fail to account for the phase shifts δ and $\delta^\pm, \varepsilon$. The second feature of importance is the loss of unitarity of the S-matrices accounted for by ρ and $\rho^\pm, \mu$. The two features are weakly coupled by the optical and reference potentials respectively. Below threshold however, a purely real optical potential and very small strengths reflect the agreement of the reference potential phase shifts with SP00. The imaginary potentials show a smooth energy dependence starting at threshold $T_{Lab} = 280$ MeV and, by having negative values, account for flux loss. Notice also that the results using inversion reference potentials (In) in the channels $^1S_0$, $^3P_0$, $^3P_1$, $^1P_1$, $^3D_2$ and $^1F_3$ have small values for the optical potential real strengths. Thus those real potentials need hardly any modifications at short distances and this supports the conjecture of the soft core potential discussed in Sect. II regarding Fig. 7. All reference potentials are most uncertain in the $^1D_2$, $^3F_3$ and $^3PF_2$ channels. This is well known as the region 300 MeV to 1 GeV is dominated by the $\Delta(1232)$ resonance while many N^* and higher spin resonances shape the region 1 to 2 GeV. Indeed the obvious energy dependences seen in the $^1D_2$ and $^3F_3$ channels are signatures of the strong coupling to the $\Delta(1232)$ resonance between $T_{Lab} = 500$ and 750 MeV. The coupled channel results shown in Fig. 14 follow closely the conclusions drawn for the single channel results. Thus only the $^1D_2$ and $^3F_3$ channels show energy dependences in the real phase shifts δ and absorptions ρ that require particular attention and an explicit treatment of resonance coupling. The $^3PF_2$ coupled channels show some similar $\Delta(1232)$ resonance coupling around 600 MeV. All the other channels support an energy independent local reference potential which can be generated by Gel'fand–Levitan–Marchenko inversion using the real phase shift

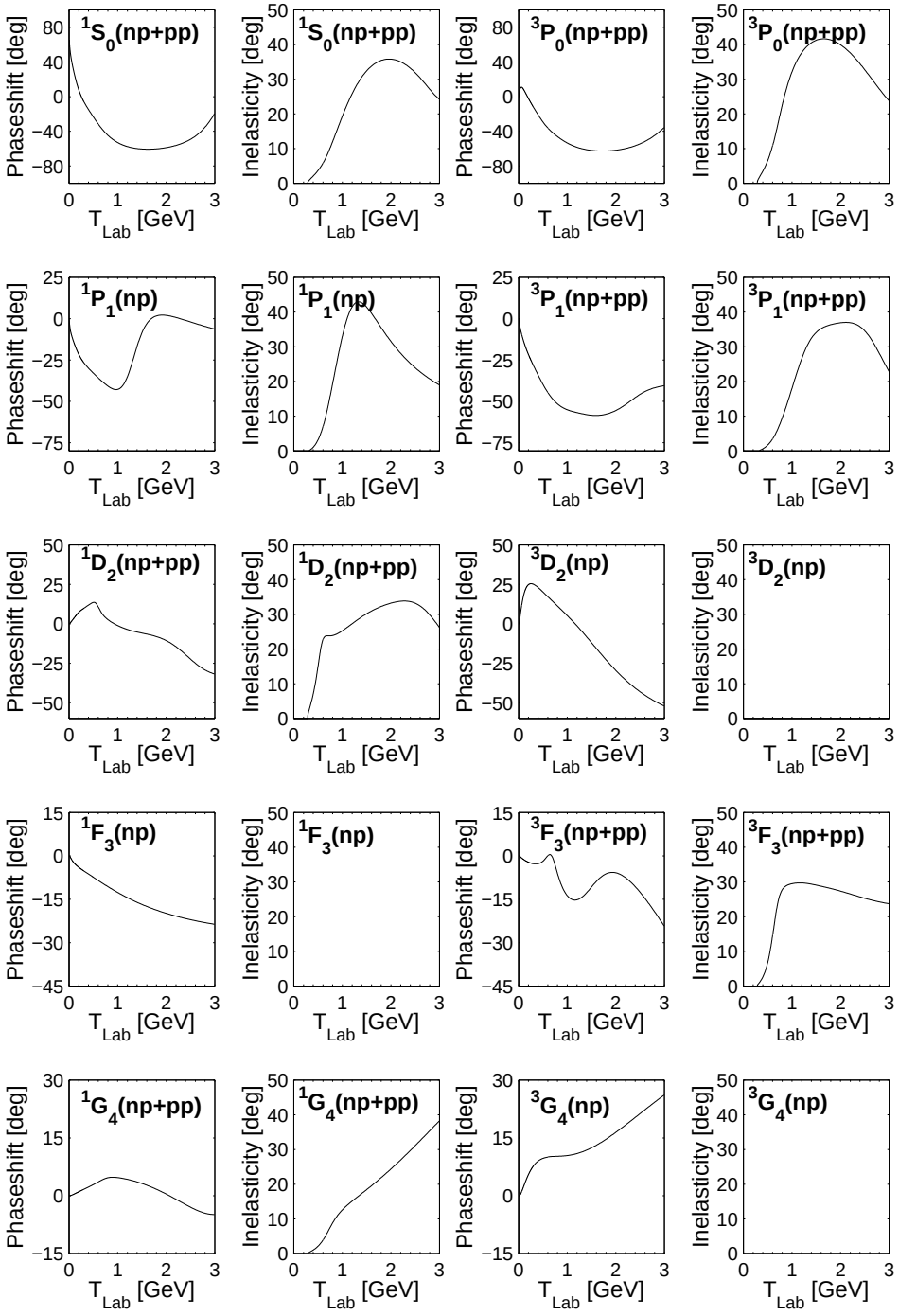

Figure 11: SP00 phase shifts for *np* single channels.

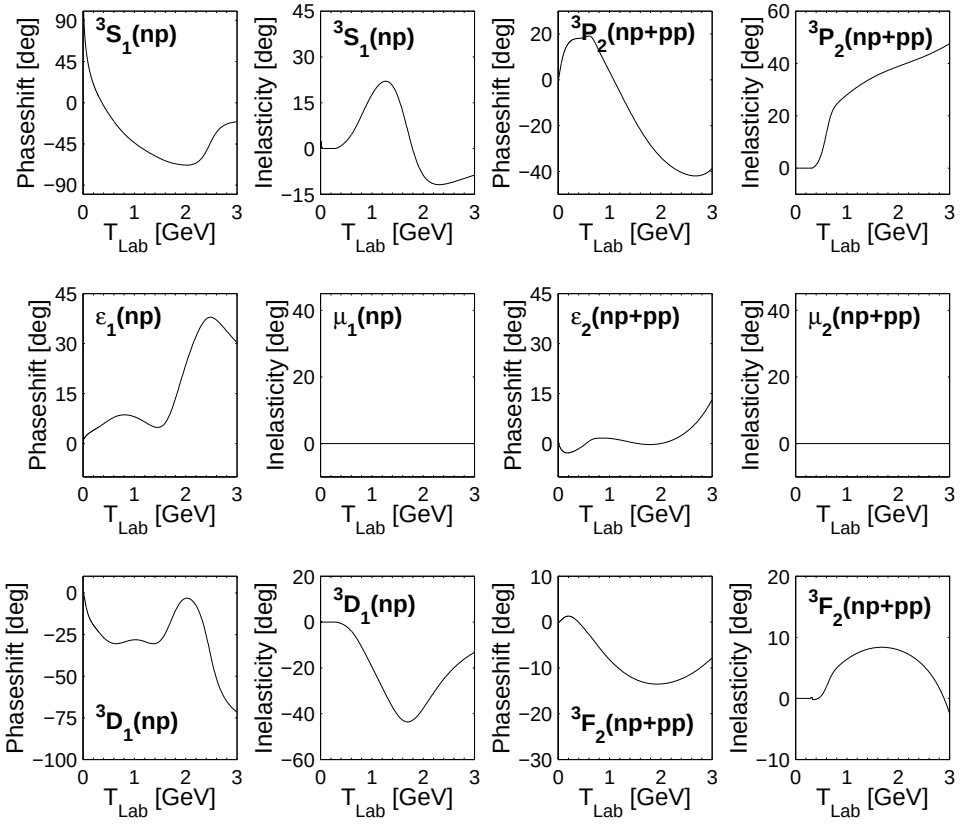

Figure 12: SP00 phase shifts for np coupled channels.

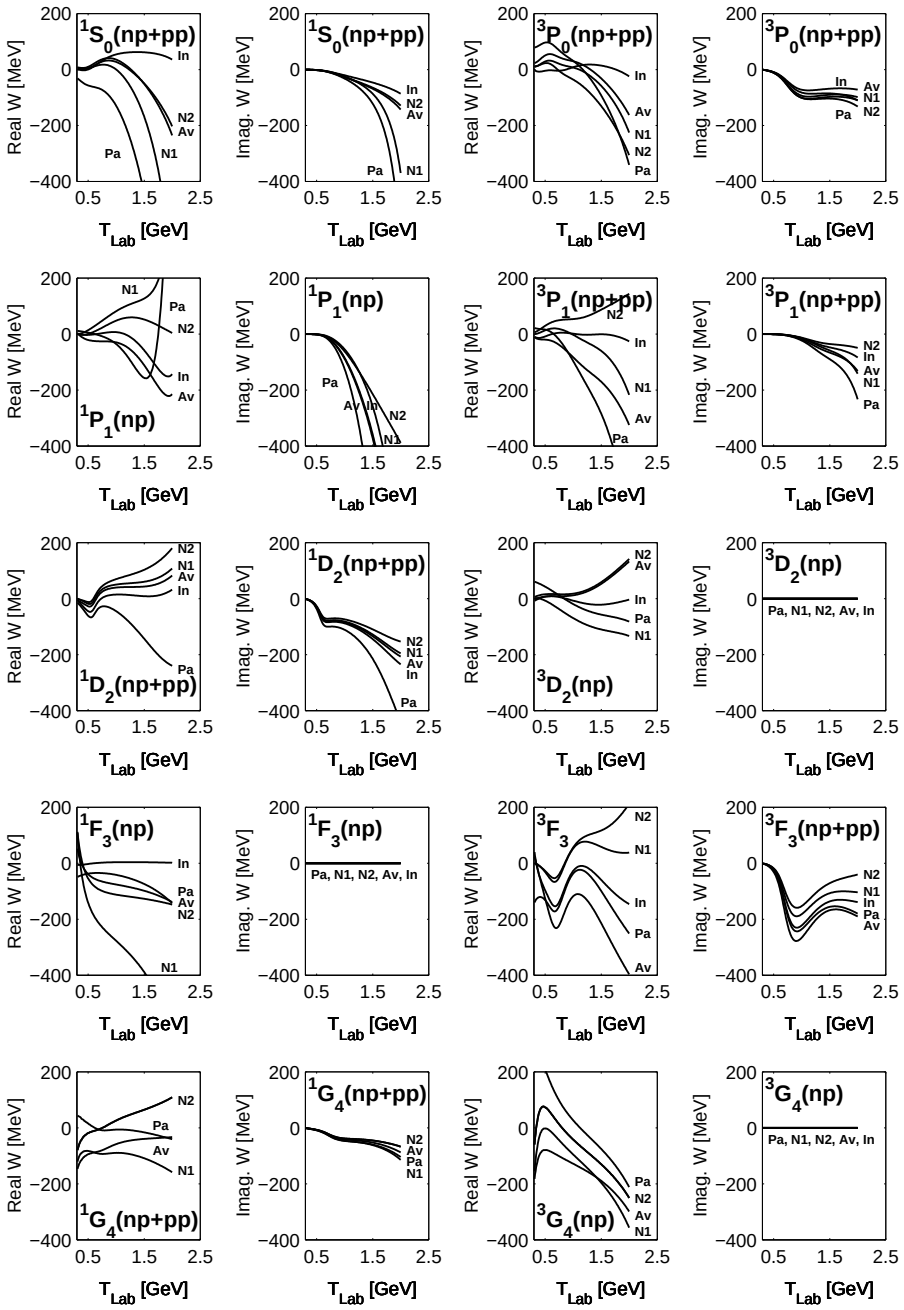

Figure 13: *np* single channel separable potential strengths, using inversion (In), Paris (Pa), Nijmegen (N1, N2) and Argonne AV18 (Av) as reference potentials with $\hbar\omega = 450$ MeV.

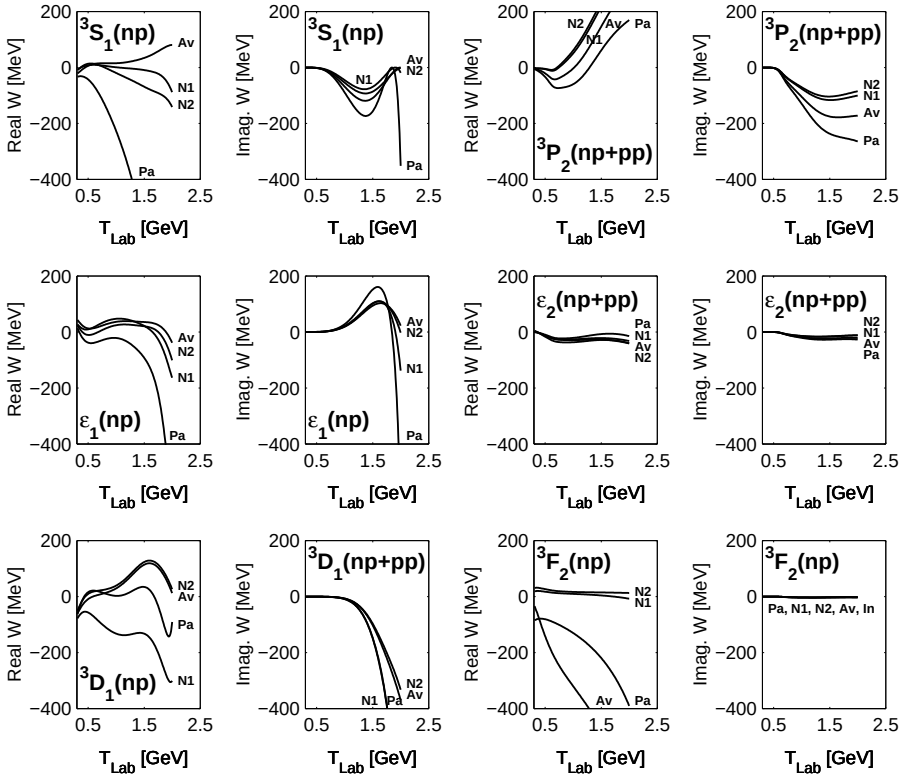

Figure 14: np coupled channel separable potential strengths, using Paris (Pa), Nijmegen (N1, N2) and Argonne AV18 (Av) as reference potentials with $\hbar\omega = 450$ MeV.

data. Also, as the optical potential strengths vary smoothly with energy for these channels, use of a complex but local very smoothly energy dependent complex potential with Gaussian or Yukawa form factors is suggested [16]. It may be that within QCD hybrid models such a *local background optical potential* can be formulated microscopically and be linked with the high energy diffraction and Regge models of elastic scattering [7, 13, 14, 38].

In addition to those optical model potentials found by using $\hbar\omega = 450$ MeV, calculations where also made using $\hbar\omega = 750$ and 900 MeV. This increase in $\hbar\omega$ reduces the range r_0 from $0.61 \rightarrow 0.47$ and $\rightarrow 0.43$ fm respectively. The primary purpose of those calculations was a search of the effective radial domain in which the reference potentials all differ most markedly. A shorter range of the form factor Φ_α leads to increased values of the optical potential strengths and thus the shortcomings of the reference potentials are magnified. To interpret this magnification, one must bear in mind the boundary condition on wave functions to be zero at the origin and the influence of a potential in the short range region, between $0 < r < 0.8$ fm for the results found using $\hbar\omega = 450$ MeV and $0 < r < 0.5$ fm in the case of $\hbar\omega = 750$ MeV. Of note in these calculations is that only on using the inversion potentials as reference do the real optical model strengths remain small. Given that the inversion potentials were designed by themselves to give the SP00 real phase shifts up to $T_{Lab} = 3$ GeV as derived from the real parts of the K-matrix Eq. (3), that aspect lends further support for a decoupling of the real and imaginary parts of the optical model potentials in calculations. Interference effects are small with the implication that the real and imaginary parts might be independently assessed. Such is not so evident when the OBEP are used as the reference potentials and the particular poor extrapolations one finds on using the Paris and Nijmegen-I that have explicit momentum dependences are most noticeable.

The $^1D_2$ and $^3F_3$ channel results are exceptional. Even with the inversion potentials as reference, the modulating optical potentials have comparable real and imaginary parts. Such reflect the means by which the optical model accounts for specific strong resonance effects.

The changes wrought in complex potential correction strengths when any OBEP is used as reference and when the $\hbar\omega$ for the defining optical potential correction form factors is enlarged to 750 and 900 MeV respectively, further stresses that any are poor choices as reference as one forces their *propriety* to even shorter ranges. In sum such have scant credibility in the range $0.5 < r < 1$ fm.

Our studies support the conceptualization of the formation and fusion of two nucleons, more generally of two elementary particles like πN, $\pi\pi$, *etc.*, into a combined object [17]. Such is correlated with selective enhancements of *probability density* and with *loss of flux* from the elastic scattering channel. The probability density of the full problem is

$$\rho_\alpha(r,k) = \frac{1}{r^2}\ Trace\ \Psi^\dagger_\alpha(r,k)\Psi_\alpha(r,k) \tag{80}$$

and the flux loss function, which results from the continuity equation $\partial_t \rho_\alpha(\mathbf{r}) + (\nabla \cdot \mathbf{j})_\alpha = 0$

and the time dependent Schrödinger equation, is

$$(\nabla \cdot \mathbf{j})_\alpha = \frac{i}{\hbar}\frac{1}{r^2} Trace \int_0^\infty \{\Psi^\dagger_\alpha(r,k)\mathcal{V}_\alpha(r,r_1)\Psi_\alpha(r_1,k) - \Psi^\dagger_\alpha(r_1,k)\mathcal{V}^\dagger_\alpha(r_1,r)\Psi_\alpha(r,k)\}dr_1. \quad (81)$$

For several low partial waves, in Fig. 15 we show probabilities as defined by Eq. (80) and flux loss via Eq. (81). In this figure the SP00 phase shift functions $\delta(T_{Lab})$ and $\rho(T_{Lab})$ are given as well for each channel and they are compared with the scatter of single energy solutions of SP00. The inversion potential phase shifts are given as well. We show these single energy solutions to acknowledge their scatter about the smooth SP00 solutions. Those sharp variations have been considered [11] as evidence of narrow dibaryon resonances. Should they be so, we contend that our potential model and associated viewpoint of fusion is still appropriate on geometric grounds. Such dibaryonic resonance effects require a detailed QCD description of their structure and decay.

The contour plots give the probability distributions and the zonal flux losses for $0 < r < 2$ fm and $T_{Lab} < 3$ GeV. From these contour plots we envisage a smooth development with energy for scattering in all channels with possible exception of the $^1P_1$, $^1D_2$ and $^3F_3$ channels. Of those, the $^1P_1$ channel is bound by data only to 1.2 GeV, above this value the SP00 phase shift function is conjecture. Nevertheless we have used the solution to demonstrate what implication such a drastic variation of $\delta(T_{Lab})$ for $1 < T_{Lab} < 2$ GeV causes in the probability distribution leaving the flux loss essentially invariant.

The $^1S_0$ and $^3P_0$ results are given in Fig. 15. They have very similar characteristics. The SP00 continuous energy solutions have phase shifts whose real parts have a minimum at about 1.6 GeV. The probability and flux loss plots show characteristic strongly distorted structures with the short distance $0.25 < r < 0.6$ fm attributes indicative of a large width ($\Gamma < 1$ GeV) resonance with strong absorption. The $^3P_1$ results given in the bottom half of Fig. 15 are interpreted similarly. The $^1P_1$ results shown in this figure have more variation as the resonance impact in the SP00 solution is reflected in the flux loss plot in particular. The $^1D_2$ and $^3F_3$ channel results are given in Fig. 15. Concomitant with the structured SP00 phase shift functions the probability plots indicate a change from the characteristic smoothness of the other channels with notable features for $400 < T_{Lab} < 900$ MeV. A very long ranged probability peak with strong distortions and significant absorption extending beyond 1 fm is evident.

The details shown are not independent of the chosen geometry of the optical potential but the patterns are quite stable with variations of the HO energy. These results support our pictorial conjectures of reaction schemes given in Figs. 5, 9 and 10. The energy dependence indicates that in the energy regime 300 MeV to 1 GeV the concept that one or the other of the colliding hadrons at most is excited to form the Δ-resonance while the two hadrons remain as disparate entities. At higher energies, and for smaller radii, the strong absorption is consistent with a fusion of the colliding particles.

The Kowalski–Noyes f-ratios of the half off-shell t-matrices

$$f_\alpha(k,q) = \frac{T^{(\pm,0)}_\alpha(T_{Lab}(k),k,q)}{T^{(\pm,0)}_\alpha(T_{Lab}(k),k,k)} \quad (82)$$

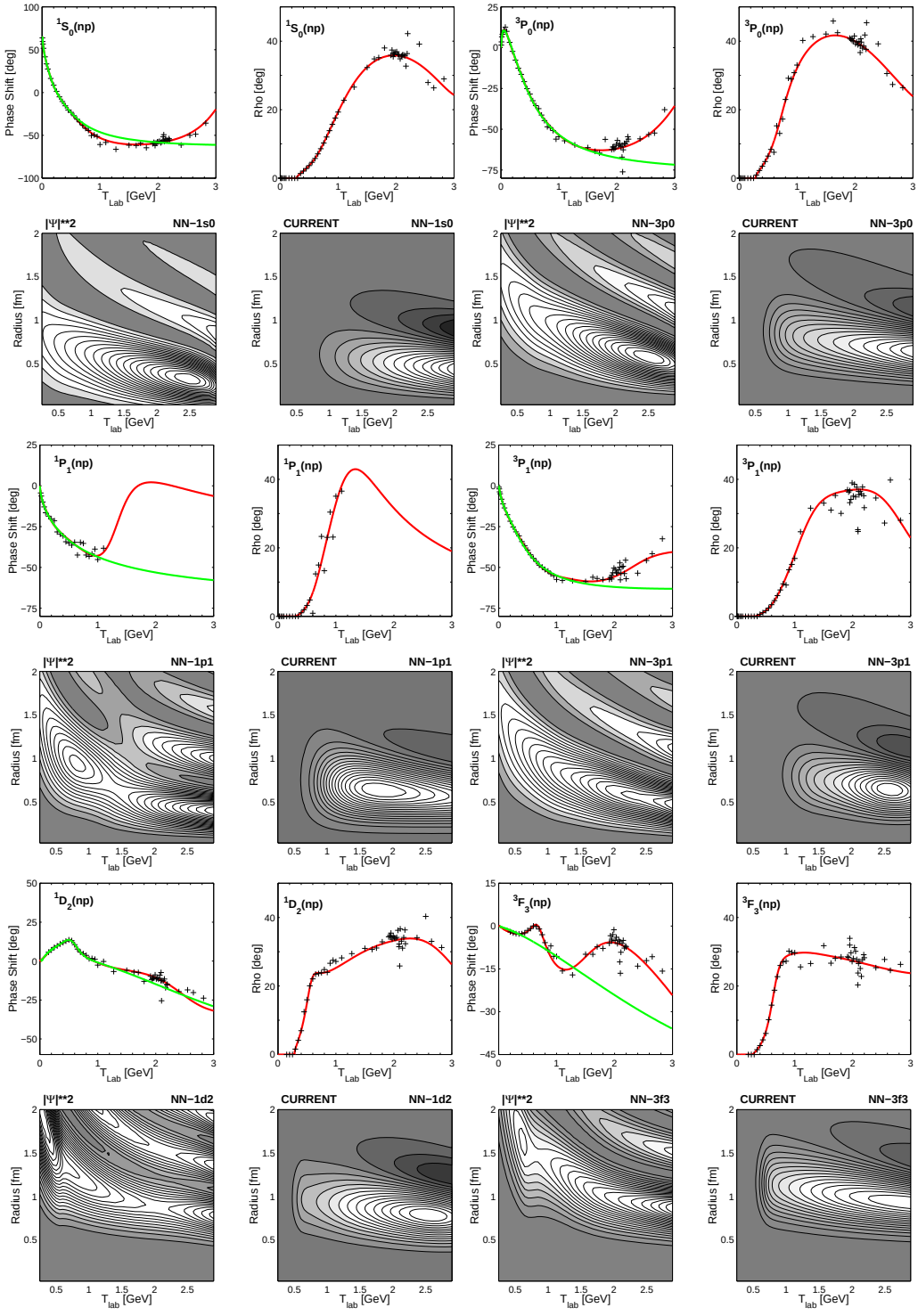

Figure 15: Block matrices containing $\delta(T_{Lab})$ and $\rho(T_{Lab})$ of SP00, and energy versus radius the probability and flux loss.

are useful quantities as they stress the potential differences in momentum space. For a purely real potential the Kowalski–Noyes f-ratio is real but this is no longer the case for complex potentials. Nevertheless, the f-ratios are always independent of the boundary conditions used in Eq. (54) to determine $T_\alpha^{(\pm,0)}(k^2,k,q)$. We show in Fig. 16 a contour plot of the $^1D_2$ and $^3F_3$ channels for T_{Lab} from 300 MeV to 1 GeV and off-shell momenta $q = k_{off}$ from 0 to 7 fm^{-1}. The Nijmegen-II and inversion reference potentials are used with these calculations.

The $^1D_2$ and $^3F_3$ channels were selected specifically as they are noticeably influenced by the Δ (1232) resonance. They also have the most drastic variations of optical potentials with the choice of reference potential. The results support our expectations, associated with strong energy dependences and/or large differences of experimental and reference potential phase shifts, which led to a scattering scheme shown in Fig. 9. It is not difficult to foresee great problems in microscopic analyses which attempt to describe the interferences between background and resonance scattering, and which aim for a unique high quality result.

For energies above 1 GeV no obvious resonance effect can be identified with elastic scattering phase shifts. However, this smoothness does not imply that the off-shell t-matrices are independent of the choice of optical potential parameterization. In Fig. 17 we show in the complex plane several Kowalski–Noyes f-ratios for the $^3P_0$ channel. In three cases we used HO form factors with $\hbar\omega = 450$, 750 and 900 MeV, and in one case we used a *normalized edge function* ($r_0 = 0.45$ fm, $h = 0.015$ fm) of Sect. III.B as boundary condition. Quite similar results were found for the other channels and the off-shell differences between these results are significant. But the influences of such large and obvious off-shell differences disappear when those off-shell t-matrices are used in few- and many-body calculations [18]. It is generally argued that only near on-shell values enter in few- and many-body calculations and symmetric sampling around the on-shell point implies that any effects of such differences are annulled. Thus we do not expect medium energy few- and many-body calculations to be more revealing than were the results of calculations at low energy. We consider it not opportune to seek or nominate a preference for any of the off-shell t-matrices or particular form factors.

5 Summary and conclusions

Diverse nucleon-nucleon r-space potentials, that yield quality fits to NN scattering phase shifts for energies below 300 MeV, have been extended to be NN optical potentials from which the SP00 phase shift functions to 3 GeV are matched. Complex short range separable potentials, addressed as the optical model potential and distinguished from the real reference potentials, bridge the gap between the experimental and reference potential phase shifts. By extending boson exchange motivated NN potential models to be optical models we invoke a new reaction scheme. At medium energy, 300 MeV to 1 GeV, this approach identifies intrinsic excitation of isolated nucleons without their fusion. At higher energies, and in particular for energies $T_{Lab} > 2$ GeV, the two nucleons can fuse into a compound system, from which meson production and other reactions eventuate, as can condensation back into the elastic channel. This view is based

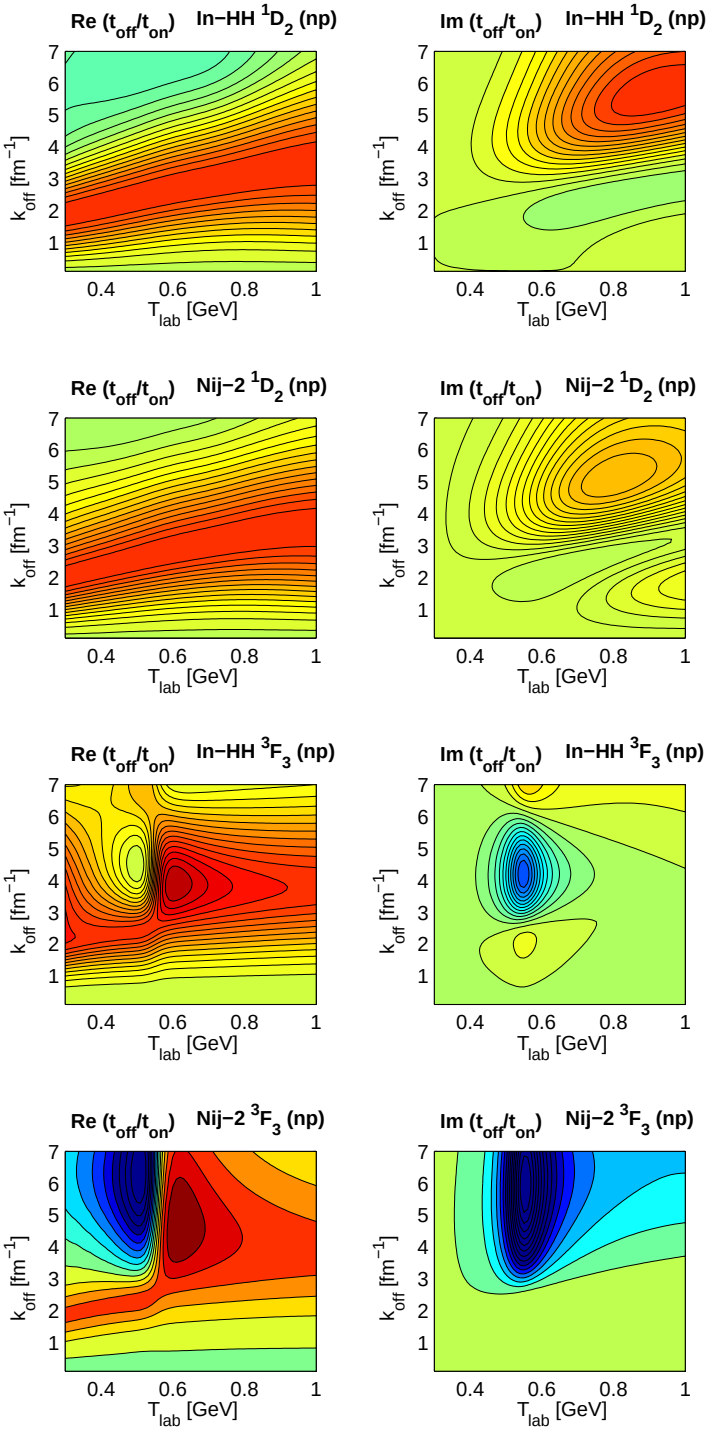

Figure 16: Kowalski-Noyes f-ratios, real part in left column and imaginary part in right column, for the ${}^1D_2$ and ${}^3F_3$ channels calculated with inversion-HH and Nijmegen-II reference potentials and optical potentials using HO, $\hbar\omega = 450$ MeV, separable form factor.

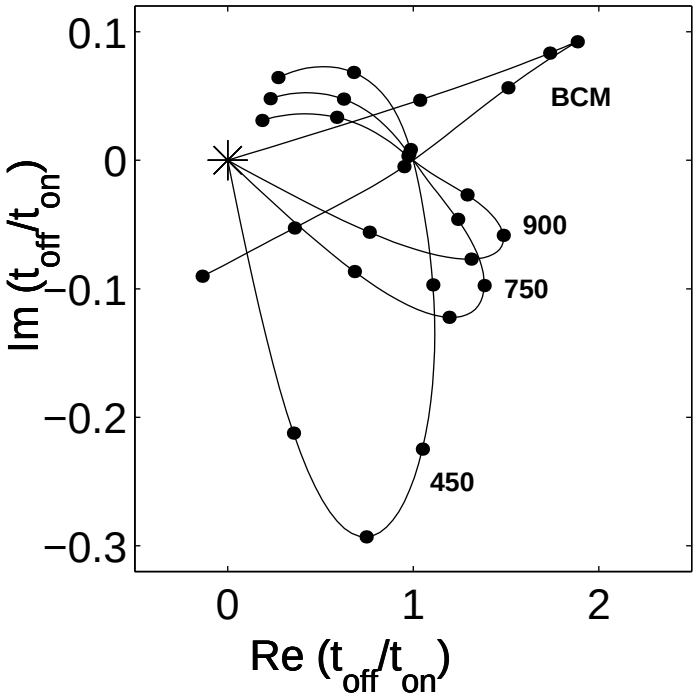

Figure 17: Kowalski-Noyes f-ratios for the $^3P_0$ channel calculated with Nijmegen-II as reference potential and optical potentials using HO $\hbar\omega$ = 450, 750, 900 MeV, and a normalized edge function (BCM) separable form factor. The dots on the curves fall onto integer k_{off} values and k_{on} is that for T_{Lab} = 2 GeV.

upon the character of the ${}^1S_0$ and ${}^3P_{0,1}$ partial wave phase shifts. Notably it is the minimum in the real phase shifts of these channels which transform into soft core potentials. The reaction volume of the fused system fits well within a sphere with radius 1 fm and the medium and long range boson exchange contributions are small corrections at best. While data at even higher energies may indicate a similar reaction scheme with the higher partial waves, it must be borne in mind that the centripetal barrier screens that scattering so reducing markedly the probability of fusion.

In the 300 MeV to 1 GeV regime, the Δ-resonance dominates ${}^1D_2$, ${}^3F_3$ and ${}^3PF_2$ partial waves and all reference potentials require large and strongly energy dependent contributions from the optical potential. Our results complement the view that this resonance must be treated explicitly. In our case, the Δ generates a doorway state to pion production and should be treated as such within the NN potential model generalization. The separable optical potential was chosen to accommodate doorway state formation and decay within a small energy region.

The OBE reference potentials presently available either give results too far from reality to qualify as background phase shifts or use the Δ-resonance in a way that prohibits separation from the background. However, by dint of their construction, inversion algorithms will help resolve these issues. The approach is such that one may start with any desired phase shift function as input. Of these any real part may be taken as the reference potential phase shifts, whose use as input to Gel'fand–Levitan–Marchenko inversion give the reference potentials themselves. Therewith, the inversion algorithm we have developed herein can then be used to determine the remaining parts of the full NN optical potential. This algorithm facilitates specification not only of complex separable potentials, appropriate for specific doorway state effects, but also of local complex potentials which encompass smooth energy dependent processes that contribute to medium to high energy NN data. The geometric attributes of the optical model, in particular the inherent soft core nature of potentials, thus have been determined solely from data. Detailed interpretation of these emergent results, of course, must eventuate from QCD inspired models.

Acknowledgement

This research was supported in part by an ARC grant.

References

[1] H. Feshbach, *Theoretical nuclear physics: Nuclear reactions*, Wiley, New York (1992).

[2] R. Machleidt, Adv. in Nucl. Phys. **19**, 189 (1989); XVIIth European Conf. on Few-Body Problems in Physics, Evora, Portugal, September 2000, arXiv: nucl-th/0009055, and to be published in Nucl. Phys. **A**.

[3] R. Machleidt and I. Slaus, arXiv: nucl-th/0101056, J. Phys. G: Nucl. Part. Phys. (2001) (in press).

[4] F. Myhrer and J. Wroldsen, Rev. Mod. Phys. **60**, 629 (1988); A.M. Kusainov, V.G. Neudatchin, and I.T. Obukhovsky, Phys. Rev. C **44**, 2343 (1991).

[5] N. Polyzou, Phys. Rev. C **58**, 91 (1998); H. Kamada and W. Gloeckle, Phys. Rev. Lett. **80**, 2547 (1998); T. W. Allen, G. L. Payne, and W.N. Polyzou, Phys. Rev. C **62**, 054002 (2000).

[6] V.I. Kukulin, V.N. Pomerantsev, A. Faessler, A.J. Buchmann, and E.M. Tursunov, Phys. Rev. C **57**, 535 (1998).

[7] S.N. Jena, P. Panda, and T.C. Tripathy, Phys. Rev. D **63**, 014011 (2000).

[8] K.A. Scaldeferri, D.R. Phillips, C.-W. Kao, and T.D. Cohen, Phys. Rev. C **56**, 679 (1997); D.B. Kaplan, M.J. Savage, and M.B. Wise, Phys. Lett. **B424**, 390 (1998); S.R. Beane, T.D. Cohen, and D.R. Phillips, Nucl. Phys. **A632**, 445 (1998).

[9] K.G. Richardson, University of Manchester Ph.D. thesis 2000, arXiv: hep-ph/0008118.

[10] R.A. Arndt, *et al.*, Phys. Rev. D **28**, 97 (1983); *ibid.* D **35**, 128 (1987); D **45**, 3995 (1992); Phys. Rev. C **49**, 2729 (1994); *ibid.* C **50**, 2731 (1994); C **56**, 3005 (1997).

[11] J. Bystricky, C. Lechanoine-Leluc, and F. Lehar, J. de Physique. **48**, 199 (1987); *ibid.* **48**, 985 (1987); **48**, 1273 (1987); **51**, 2747 (1990); C. Lechanoine-Leluc and F. Lehar, Rev. Mod. Phys. **65**, 47 (1993); C.E. Allgower, *et al.*, Nucl. Phys. **A637**, 231 (1998); Phys. Rev. C **60**, 054001 (1999); *ibid.* C **60**, 054002 (1999); C **62**, 064001 (2000).

[12] R.A. Arndt, I.I. Strakovsky, and R.L. Workman, Phys. Rev. C **62**, 034005 (2000).

[13] S.Y. Lo, *Geometrical pictures in hadronic collisions*, World Scientific, Singapore (1987).

[14] G. Matthiae, Rep. Prog. Phys. **57**, 743 (1994); P.V. Landshoff, summary talk at Diffraction 2000, Centraro, Italy, arXiv: hep-ph/0010315.

[15] V.G. Neudatchin, N.P. Yudin, Y.L. Dorodnykh, and I.T. Obukhovsky, Phys. Rev. C **43**, 2499 (1991).

[16] H.V. von Geramb, K.A. Amos, H. Labes, and M. Sander, Phys. Rev. C **58**, 1948 (1998).

[17] H.V. von Geramb, A. Funk, and A. Faltenbacher, Proc. Sarospatak Int. Workshop, Sept 2000, Hungary, to appear in Few-Body Systems Suppl., Springer (2001).

[18] K. Amos, P. J. Dortmans, H. V. von Geramb, S. Karataglidis, and J. Raynal, Adv. in Nucl. Phys. **25**, 275 (2000).

[19] Th. Kirst, J. Math. Phys. **32**, 1318 (1991).

[20] R. Machleidt, Phys. Rev. C **63**, 024001 (2001).

[21] L. Jäde, Phys. Rev. C **58**, 98 (1998).

[22] M. Lacombe, B. Loiseau, J.M. Richard, R. Vinh Mau, J. Côté, P. Pirès, and R. de Tourreil, Phys. Rev. C **21**, 861 (1980).

[23] V.G.J. Stoks, R. Timmermans, and J.J. de Swart, Phys. Rev. C **47**, 512 (1993); *ibid.* C **48**, 792 (1993); C **49**, 2950 (1994).

[24] R.B. Wiringa, V.G.J. Stoks, and R. Schiavilla, Phys. Rev. C **51**, 38 (1995).

[25] T. Kirst, *et al.*, Phys. Rev. **C 40**, 912 (1989); H.V. von Geramb and H. Kohlhoff, in *Quantum Inversion Theory and Applications*, Lect. Notes in Physics **427**, Springer (1994).

[26] M. Sander and H.V. von Geramb, Phys. Rev. C **56**, 1218 (1997).

[27] V.G.J. Stoks, R.A.M. Klomp, M.C.M. Rentmeester, and J.J. de Swart, Phys. Rev. C **48**, 792 (1993), The phase shift data are available from `http://nn-online.sci.kun.nl`.

[28] R.A. Arndt, W.J. Briscoe, R.L. Workman, and I.I. Strakovsky, CNS DAC [SAID], Dept. of Physics, The George Washington University, `http://gwdac.phys.gwu.edu/`.

[29] R.A. Arndt and L.D. Roper, Phys. Rev. D **25**, 2011 (1982).

[30] D. Hadjimichef, J. Haidenbauer, and G. Krein, Phys. Rev. C **63**, 035204 (2001).

[31] H. Feshbach, Ann. Phys. (N.Y.) **281**, 519 (2000); *ibid.* **165**, 398 (1985).

[32] R. Blankenbecler and R. Sugar, Phys. Rev. **142**, 1051 (1966).

[33] F. Gross, J.W. Van Orden, and K. Holinde, Phys. Rev. C **45**, 2094 (1982); A. Amghar, B. Desplanques, and L. Theussl, arXiv: nucl-th/0012051 (2000); G. Ramalho, A. Arriaga, and M.T. Pena, arXiv: nucl-th/0012086 (2000); C. Savkli and F. Gross, Phys.Rev. C **63**, 035208 (2001).

[34] M.H. Partovi and E.L. Lomon, Phys. Rev. D **2**, 1999 (1970).

[35] N.H. Kwong and H.S. Köhler, Phys. Rev. C **55**, 1650 (1997).

[36] J. M. J. van Leeuwen and A. S. Reiner, Physica **27**, 99 (1961); M.G. Fuda and J.S. Whiting, Phys. Rev. C **8**, 1255 (1973).

[37] J. Raynal, in *The structure of nuclei*, IAEA, Vienna (1972), *computer code DWBA91*, NEA 1209/02 (1999); and *private communication*.

[38] P.D.B. Collins, *An Introduction to Regge Theory and High Energy Physics*, Cambridge University Press (1977).